

1 **The Importance of Lateral Variability on Exchange Across the**
2 **Inner Shelf South of Marthas Vineyard, MA.**

3 **A. R. Kirincich^{1*}, S. J. Lentz¹**

4 ¹Department of Physical Oceanography, Woods Hole Oceanographic Institution, Woods Hole, Massachusetts, USA.

5 **Key Points:**

- 6 • Exchange across the inner shelf south of Martha’s Vineyard, MA is driven by a com-
7 plex combination of non-uniform, wind-driven depth-dependent exchange, coherent ed-
8 dies, and a spatially varying background circulation.
- 9 • While components of the depth-dependent across-shelf exchange were correlated with
10 simple estimates of the wind-driven exchange, the integrated transport observed over
11 the summer stratified period was often opposite the direction of the wind-driven exchange.
- 12 • A vigorous field of coherent submesoscale eddies, observed with time and space scales
13 generally shorter than 10 hours, smaller than 6 km, and shallower than 10 meters, were
14 responsible for volume exchange equal to more than half that of the wind-driven depth-
15 dependent transport.

*

Corresponding author: A. R. Kirincich, akirincich@whoi.edu

Abstract

Lateral variations in inner-shelf circulation have the potential to augment the across-shelf exchange primarily driven by the wind. This study uses a combination of high-resolution HF radar-based surface currents and a dense array of moorings south of Martha's Vineyard, MA to document the lateral variability present on the inner shelf and quantify its importance to across-shelf exchange. Averaged over an along-shelf scale of 14 km, the cumulative wind-driven across-shelf transport over the summer was less than the volume of the inner-shelf onshore of the 25-m isobath. Along-shelf variations in the wind-driven exchange were as large as the spatial mean. Independent of the wind forcing, a spatially varying time-averaged circulation, driven by a combination of tidal rectification and horizontal density gradients, resulted in along-shelf density variability, and across-shelf exchange larger than that due to wind forcing. Coherent submesoscale eddies also occurred frequently within the domain due to flow-topography effects onshore and horizontal density gradients offshore, generally with lifespans shorter than 10 hours, diameters smaller than 6 km, and vertical depths shallower than 10 meters. The across-shelf volume transport due to eddies, estimated by seeding particles within the surface current fields, was more than half the wind-driven depth-dependent exchange. Thus, accounting for the potential coherent along-shelf variability present over the inner-shelf can significantly increase estimates of the across-shelf transfer of water masses and particles.

1 Introduction

Visible beyond the surf zone, the inner part of the continental shelf serves as a connector between the nearshore, dominated by breaking waves, and the larger coastal ocean over the horizon, dominated by geostrophic and larger scale motions [Lentz, 2001]. The dynamics that control circulation in this region are decidedly different from that occurring both onshore and offshore [e.g. Allen, 1980; Lentz and Winant, 1986; Lentz et al., 1999] and yet critical to predicting the exchange across it. How this exchange occurs and what processes drive it effects the transport of water masses, nutrients, pollutants, and larval fish or invertebrates [e.g. Menge et al., 2003; McGillicuddy et al., 2005; Dudas et al., 2009] between the coastal ocean to the nearshore. While depth-dependent wind-driven upwelling or downwelling exchange has been quantified in detail [Lentz, 2001; Kirincich et al., 2005; Tilburg, 2003; Fewings et al., 2008; Lentz et al., 2008; Fewings and Lentz, 2011, among others], the role of lateral variability in modifying this exchange is poorly understood because of the difficulty of observing lateral variability at short scales using conventional mooring-based techniques. This study examines the

48 spatial variability of transport within the inner shelf south of Martha's Vineyard Massachusetts,
 49 its time and space dependence, and its importance to the total volume exchanged between the
 50 nearshore and the coastal ocean.

51 Dynamically defined as the part of the shelf where the surface and bottom Ekman lay-
 52 ers overlap and interact [*Mitchum and Clarke*, 1986], the inner shelf has been studied primar-
 53 ily within a 2D, along-shelf uniform framework [see review by *Lentz and Fewings*, 2012]. Depth-
 54 dependent across-shelf transport due to wind-driven upwelling and downwelling dominate the
 55 exchange of water masses on many continental shelves [*Huyer*, 1990]. However, within the
 56 inner shelf, forcing due to across-shelf winds [*Tilburg*, 2003; *Fewings et al.*, 2008] and waves,
 57 via the Stokes-Coriolis force [*Lentz et al.*, 2008], can lead to higher magnitudes of volume trans-
 58 port than that possible via along-shelf wind-driven exchange alone, as overlapping boundary
 59 layers reduce the across-wind transport within the inner shelf *Lentz* [1994]. Further, numer-
 60 ical model results have illustrated the potential for local minima in exchange [*Austin and Lentz*,
 61 2002; *Kuebel Cervantes et al.*, 2003] within the inner shelf under along-shelf wind forcing, sug-
 62 gesting that this area of the shelf can serve as a effective barrier, isolating the nearshore from
 63 the larger coastal ocean.

64 Along the coast, even small variations in bathymetry, hydrography, or forcing (e.g. vari-
 65 ations in the wind) can lead to important deviations from the 2D picture described above. Sev-
 66 eral examples of flow-topography effects [*Song et al.*, 2001; *Tilburg and Garvine*, 2003; *Yankovsky*
 67 *and Chapman*, 1995] exist for the inner shelf and parallels to larger, shelf-scale variations [*Kir-*
 68 *incich and Barth*, 2009a; *Castelao and Barth*, 2006; *Huyer et al.*, 2005] can be made. Yet rel-
 69 ative to the depth-dependent exchange, the importance of lateral variability caused by bathy-
 70 metric features, wind forcing, or the exchange due to coherent vorticities or eddies and inco-
 71 herent horizontal stirring has not been quantified. In a general sense, numerical models of in-
 72 ner shelf flows parameterize coherent or incoherent stirring via the use of a nominally con-
 73 stant horizontal eddy diffusivity to account for the effects of unresolved horizontal motions.
 74 With typical values tracing back to *Okubo* [1971], both 3D and 2D model results realize small
 75 amounts of exchange across the inner shelf [e.g. *Austin and Lentz*, 2002] due to lateral eddy-
 76 viscosity. The lack of high resolution observations of coastal flows at horizontal scales less
 77 than a few kilometers has been a barrier towards both quantifying the effects of lateral vari-
 78 ability and improving estimates of lateral stirring and energy transfer in the coastal ocean [*Capet*
 79 *et al.*, 2008].

80 The inner shelf south of Martha's Vineyard, MA (Fig. 1) has been the site of recent ef-
81 forts to examine both the 2D exchange present and the role of lateral variability. Previous stud-
82 ies of 2D exchange dynamics made using a single across-shelf array of moorings in the re-
83 gion observed strong coherence to theoretical transport estimates based solely on the wind [*Few-*
84 *ings et al., 2008; Horwitz and Lentz, 2014*]. *Fewings and Lentz* [2011] concluded that time-mean,
85 non-wind driven upwelling circulation cooled the inner shelf south of Martha's Vineyard in
86 summer. However, numerical model analysis [*Wilkin, 2006; Ganju et al., 2011*] and high-resolution
87 HF radar-based surface current observations [*Kirincich et al., 2012*] have found that the area
88 is also subject to strong lateral gradients in tidal velocities due to the proximity of Wasque Shoals,
89 a bathymetric shoal located between the islands of Martha's Vineyard and Nantucket. These
90 lateral gradients in the tide lead to tidal rectification and a non-uniform low-frequency, or 'back-
91 ground' circulation pattern. This pattern drives both sustained lateral gradients in across-shelf
92 velocity and advective heat flux at the surface [*Kirincich et al., 2012*]. Additional analysis of
93 the HF radar-based observations used by *Kirincich et al.* [2012] identified significant numbers
94 of coherent vorticities or eddies with spatial scales of 2-5 km within a small (10×15 km) area
95 due in part to wind forcing and tidal dynamics [*Kirincich, 2016*]. While focused on the struc-
96 ture and dynamics of the eddies occurring near Wasque Shoals, *Kirincich* [2016] also suggested
97 that eddies had the potential to be an important means of lateral exchange for surface waters
98 over the inner shelf. However, without knowledge of the vertical extent of the eddies, their full
99 effect could not be quantified.

100 This study uses a combination of high-resolution HF radar surface current observations
101 and a dense array of hydrographic and velocity moorings to examine the lateral scales of vari-
102 ability present on the inner shelf south of Martha's Vineyard, MA and quantify the importance
103 of these variations in relation to depth-dependent mechanisms for volume transport across the
104 inner shelf. Relative to the surface current observations described by *Kirincich et al.* [2012]
105 and *Kirincich* [2016], the radar deployment used here covered a broader spatial extent at slightly
106 coarser spatial resolution. These data were collected during the Inner-shelf Lateral Exchange
107 (ISLE) study, which is described in detail below, followed by descriptions of the analysis meth-
108 ods used to estimate surface layer transports, identify eddies, and track particles. These data
109 are then used to describe: the background circulation during the 6-month study period, the wind-
110 driven depth-dependent exchange flow observed, and the occurrence of individual coherent vor-
111 tex features or eddies. The across-shelf transport driven by each of these processes are quan-
112 tified, and the results discussed in terms of their implications for the transport of water par-

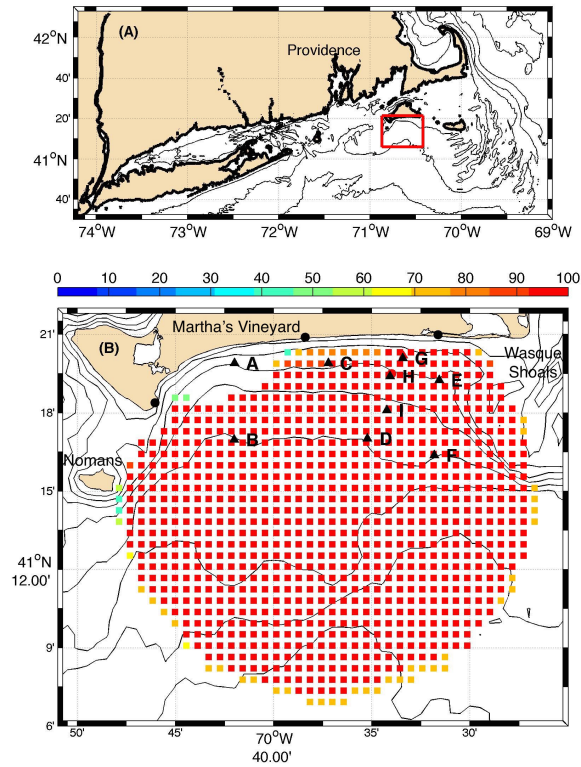
113 ticles across the Martha's Vineyard inner shelf in particular as well as inner shelves in gen-
114 eral. Thus, work focuses on the potential of wind-driven, eddy-driven, or mean processes to
115 translate water masses across the shelf in a seasonally-integrated sense, and does not include
116 the potential effects of horizontal or vertical mixing on exchange.

117 **2 Data**

118 Conducted in the summer and fall of 2014, the Inner shelf Lateral Exchange (ISLE) study
119 observed the in situ velocity and density structure at multiple locations in the inner shelf south
120 of Martha's Vineyard MA, and paired these observations with high resolution remotely sensed
121 observations of surface currents made using land-based high frequency (HF) radar systems.

122 **2.1 Subsurface Velocity and Hydrography**

123 Observations of the vertical structure of velocity and hydrography were made at 9 lo-
124 cations within the study area, spanning water depths of 12 to 25 m, 1.5 to 11.5 km offshore
125 (Fig. 1). At each location, a surface mooring supported 4 to 7 SBE-37 MicroCats measuring
126 temperature and conductivity (CT) throughout the water column (Tab. 1). A nearby bottom
127 lander supported an acoustic Doppler current profiler (ADCP) sampling water column veloc-
128 ities using vertical bins of 0.25 to 1 m and sample rates of 0.33-1 Hz. Stations A,B,C, and F
129 were deployed continuously from June 9th to December 4th while Stations E and I were de-
130 ployed for 2 shorter time periods (Tab. 1) due to the constraints of a collaborative field pro-
131 gram. The ADCP at Station D was snagged by a trawler in mid-June and redeployed on Au-
132 gust 5th. Station G is MVCO's long-term underwater node, where continuous ADCP obser-
133 vations have been available since 2001. Station H, located adjacent to the MVCO tower it-
134 self, was deployed in early August. The CT observations were processed and quality controlled
135 to minimize both temperature and conductivity spikes as well as biases due to conductivity
136 drift before being used to estimate salinity and density. ADCP along-beam velocities were pro-
137 cessed following [e.g. *Kirincich and Barth, 2009b*] to give timeseries of quality controlled, hor-
138 izontal velocities from 1 m above the instrument to 2-4 below the sea surface due to side lobe
139 interference [*Gordon, 1996*]. The exact bin of the side-lobe masking was determined using a
140 precise, signal intensity-based, estimate of the sea surface height that accounted for tidal vari-
141 ability of the water column. All moored timeseries were averaged over independent 1/2 hour
142 time intervals, centered on the hour, to match the temporal resolution of the surface current
143 observations.



144 **Figure 1.** (top) The Southern New England Shelf with the study area south of the Martha's Vineyard, Mas-
 145 sachusetts denoted in red. (bottom) HF radar % coverage map with the locations of the radar stations (dots)
 146 and the ISLE moorings (triangles).

148 2.2 Surface Currents

149 For the ISLE study, the WHOI high resolution HF radar system [Kirincich *et al.*, 2013]
 150 was reconfigured to observe surface currents within an expanded 30×40 km coverage area from
 151 May to December of 2014. The three HF radar systems were spaced at ~10 km intervals along
 152 the south coast of Martha's Vineyard (Fig. 1). Each system was a 25 MHz Codar Ocean Sys-
 153 tems SeaSonde direction-finding radar operated using a combination of 350 kHz bandwidth
 154 and low transmit power (10 W) to achieve resolutions of 429 m over ranges of 40 km. For
 155 each system, 1024 point (~8 minute) spectral estimates of the radar backscatter were used to
 156 resolve doppler velocities less than 0.01 m s^{-1} . Successive spectra were averaged using a mov-
 157 ing 24 min averaging window to form an average spectral estimate every 15 min. which were
 158 processed using advanced methods [Kirincich *et al.*, 2012; Kirincich, 2016] into quality con-
 159 trolled estimates of the radial velocity at radial and azimuthal resolution of 429 m and 5 de-

Table 1. The ISLE Mooring Array

Mooring	Location		Deployment Dates	Water			ADCP bin size (m)
	Lat.	Lon.		Depth (m)	CT Depths (m)	ADCP type	
A	41° 19.9115' N	70° 41.9909' W	06/09/2014 - 12/02/2014	15	1,3,6,9,11	WH ^a 1200 kHz	0.5
B	41° 16.9728' N	70° 42.0058' W	06/09/2014 - 12/02/2014	25	1,3,6,9,12,17,21	WH 600 kHz	1.0
C	41° 19.9113' N	70° 37.2089' W	06/09/2014 - 12/02/2014	15	1,3,6,9,11	WH 1200 kHz	0.5
D	41° 17.0233' N	70° 35.2148' W	08/05/2014 - 01/15/2015	25	1,3,6,9,12,17,21	WH 600 kHz	1.0
E	41° 19.2610' N	70° 31.5581' W	07/02/2014 - 09/22/2014	15	1,3,6,9,11	NO ^b 1000 kHz	0.25
			11/11/2014 - 01/13/2015	15	1,3,6,9,11	NO 1000 kHz	0.25
F	41° 16.3790' N	70° 31.8090' W	06/11/2014 - 12/05/2014	25	1,3,6,9,12,17,21	WH 600 kHz	1.0
G	41° 20.0931' N	70° 33.4099' W	06/09/2014 - 12/31/2014	12	1,4,6,9	WH 1200 kHz	0.5
H	41° 19.4067' N	70° 34.0606' W	08/06/2014 - 01/15/2015	16	1,3,6,9,11	NO 1000 kHz	0.25
I	41° 18.1100' N	70° 34.2297' W	07/02/2014 - 09/22/2014	21	1,3,6,9,12,17	WH 600 kHz	1.0
			11/11/2014 - 01/13/2015	21	1,3,6,9,12,17	WH 600 kHz	1.0

^a T-RDI Workhorse Mariner or Monitor, ^b Nortek 5-beam AD2CP

160 grees respectively. These data were combined into vector velocities on a uniform 800 m res-
 161 olution grid via a weighted least squares technique using data within 1 km and successive 1/2
 162 hour time intervals centered on the hour. Use of the logarithm of the estimated signal power
 163 as a weighting function increased the accuracy of the final product (App. A:) and, when car-
 164 ried through the vector calculation, served as a superior indicator of velocity quality compared
 165 to standard error estimates based on the standard deviation of the radial velocity average (Fig.
 166 A.1).

167 2.3 Ancillary data

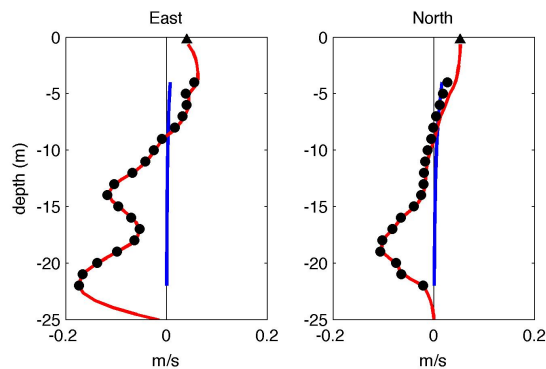
168 Wind velocities and meteorological conditions were recorded by MVCO both at a shore
 169 meteorological mast and an offshore tower (Fig. 1). Winds from the tower, measured by a 3-
 170 axis sonic anemometer located at 17 m above the sea surface, were used primarily here, and
 171 are thought to be representative of winds over the entire study area. Small gaps in the tower
 172 wind record were filled using land-based sensors using transfer functions developed by *Few-*
 173 *ings et al.* [2008]. Wind stress was estimated from the tower winds using bulk formulae [*Large*

174 *and Pond, 1981*]. Estimates of the significant wave height and dominant wave period were es-
 175 timated from the 2-Hz ADCP observations made at Station G, following *Terray et al. [1997]*.

176 3 Methods

177 3.1 Surface Layer Transport

178 The velocity profiles collected by the moored ADCPs were used to estimate the across-
 179 shelf transport within the surface layer following the methods described by [*Lentz, 2001; Kir-*
 180 *incich et al., 2005*], with a few key additions. At each mooring location, except station A, the
 181 observed HF radar surface currents nearest the location of the mooring were combined with
 182 the subsurface velocities to create a full water column velocity profile for each 1/2 hour of the
 183 full time series. At station A, which was not located within the radar coverage area, the ve-
 184 locity in the top 3 bins of the ADCP were extrapolated to the surface [following *Lentz, 2001*]
 185 to form the full water-column velocities. An estimate of the Stokes drift, which was measured
 186 by the radars but not by the ADCPs [*Kirincich et al., 2012*], was added to the ADCP obser-
 187 vations using the observed wave statistics [following *Lentz et al., 2008*]. This addition accounted
 188 for both a key difference between the HF radar and ADCP data sets and any potential wave-
 189 driven across-shelf exchange that would be seen in the ADCP results due to their Eulerian ref-
 190 erence frame. Velocities were interpolated from the highest measured bin of the ADCP to the
 191 HF radar velocity at 0.5 m depth [*Stewart and Joy, 1974*], and from the bottom-most ADCP
 192 depth bin to 0 at the bottom (Fig. 2).

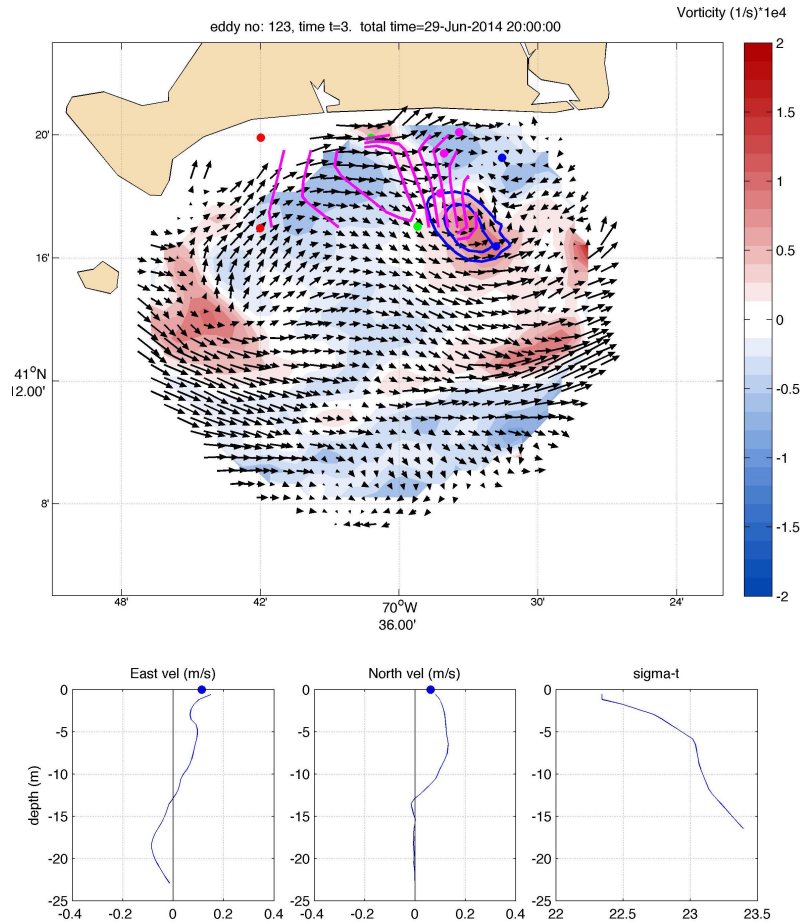


193 **Figure 2.** Sample vertical structure of the residual (tide and background mean removed) velocities incor-
 194 porating both the ADCP and HF radar observations from lander B. Shown for the (left) east and (right) north
 195 velocities are: the observed velocities from the ADCP (dots) and HF radar (triangle), the estimated Stokes
 196 drift vertical structure (blue), and the final interpolated velocity profile (red).

197 To estimate the across-shelf transport, the full water column velocity profiles were ro-
 198 tated into a coordinate system aligned with the principal axis of flow, determined using the
 199 depth-averaged velocity after an estimate of the depth-averaged tidal flow, found using 8 tidal
 200 components and T_tide [Pawlowicz *et al.*, 2002], was removed. Estimates of (1) the depth-varying
 201 tidal flow, (2) the monthly-mean vertical structure of the across-shelf velocity, and (3) the depth-
 202 averaged across-shelf velocity were made and subtracted from the across-shelf velocities to
 203 obtain the across-shelf velocity anomaly at each station. The time-varying across-shelf sur-
 204 face transport was estimated by integrating the velocity anomaly from the surface to the first
 205 zero-crossing of the profile (Fig. 2) deeper than 2 m depth and assuming a unit along-shelf
 206 width to yield timeseries of surface layer transport (U_{obs} , in m^3/s per along-shelf m) at each
 207 station. Tests comparing the surface transport results with and without the HF radar-based ex-
 208 trapolation to the surface found that, despite the potential noise in the radar observations, ac-
 209 counting for the near-surface shear increases correlations with the theoretical wind-driven trans-
 210 ports (shown below) by an average of 0.1 and 0.15 in summer and winter respectively.

211 3.2 Coherent Eddies

212 Following a methodology described in detail by Kirincich [2016] and Kim [2010], this
 213 work defines an eddy as a set of closed contours of the stream function formed by the non-
 214 divergent horizontal stream function. The stream function and non-divergent velocities were
 215 isolated using a least squares fit to each independent 1/2 hour residual velocity estimate –with
 216 the tide and temporal mean removed [Kirincich, 2016] –accounting for $70\% \pm 10\%$ of the east
 217 velocity and $60\% \pm 10\%$ of the north velocity components. The stream function interval used
 218 to find the eddy field was fixed at $\delta\psi = 50 \text{ m}^2 \text{ s}^{-1}$ units for the data set (Fig. 3). This defines
 219 the minimum circulation of an eddy, and is based on the potential error of the HF radar ve-
 220 locity estimates, generally 6 cm s^{-1} over the 800 m grid spacing (App. A:). The method iden-
 221 tifies only features that exceed a minimum change in streamfunction (i.e. intensity) that are
 222 larger than a minimum size (6 grid points for an effective minimum radius of ~ 2 km) and can
 223 be observed for longer than a minimum time period (1.5 hours or three 1/2 hour observations).
 224 The effective radius of the eddy was defined as the radius of a circle with an area equal to the
 225 area of the eddy. The center of the eddy was defined as the local minima or maxima of the
 226 stream function within the eddy. Eddies were tracked over time following [Chelton *et al.*, 2011].



227 **Figure 3.** (top) Example of surface current velocity product (vectors) obtained on June 29th, 2014 at 20:00
 228 UTC. Overlaid on the vectors are the defined eddy streamlines (blue contours), vorticity (color), and den-
 229 sity (magenta contours with contour interval of $\sigma=0.02$). (bottom) The vertical structure of the (left to right)
 230 east velocity, north velocity, and density measured at Lander F during the time of the eddy. In the example
 231 shown, an eddy depth of 12 m was determined using the veering of the velocity vector from the surface as the
 232 defining criteria (see text).

233 3.3 Eddy Depths

234 The full velocity profiles available at the moorings were used to estimate the vertical struc-
 235 ture of eddies when eddies were observed to pass over a mooring. For each realization of an
 236 eddy at a mooring, the vertical extent of the eddy was determined from the veering angle of
 237 the horizontal velocity profile with depth below the surface. The depth at which the velocity
 238 veered more than 90 degrees from the direction of the observed surface current was assumed
 239 to be representative of the thickness of the eddy itself. All available estimates of the eddy depth

240 over the eddy lifespan were averaged to estimate the mean eddy depth. Additionally, the time-
241 averaged eddy depth with radial distance away from the center of the eddy was estimated by
242 tracking the eddy in an eddy-following coordinate system, and normalizing the distance to the
243 center by the instantaneous effective radius of the eddy. Despite the dense spacing of the moor-
244 ings, the number of eddies passing moorings was not sufficient to realize useful statistics on
245 the change in depth of the eddy over its lifespan or the full horizontal variability of the eddy
246 depth for individual eddies. The method used here was compared to methods using: differ-
247 ent veering cutoffs (i.e 45°), the depth to the first zero crossing of the dominant velocity com-
248 ponent (Fig. 3), and a change in density cutoff to define the eddy thickness. In general, velocity-
249 based criteria were found to have reduced standard deviations for most eddy types (see be-
250 low) than density-based estimates, and while differences existed in the absolute eddy depth
251 results for individual threshold levels, the relative differences between eddy types were con-
252 sistent across all methods.

253 **3.4 Eddy Transport**

254 Finally, the trajectories of pseudo-particles seeded within the surface current results are
255 used to track the movement of particles starting within coherent eddies, as well as establish
256 the potential for transport across the shelf [*Rypina et al.*, 2016; *Kirincich*, 2016]. Particle track-
257 ing, utilizing the *HFR_Progs* Matlab toolbox which follows *Kaplan and Largier* [2006], was
258 done for each eddy using two separate pseudo-deployments: (1) Particles starting within co-
259 herent eddies that overlap the 25-m isobath, and (2) particles starting along a line passing through
260 the center of each eddy, and advected over the lifespan of the eddy. In each case, the trajec-
261 tories are assumed to be representative of a volume of water equivalent to an HF radar grid
262 point in area (800×800 m) with a vertical extent equal to the mean eddy depth. The integrated
263 northward (effectively onshore) volume transport of the pseudo-trajectories are used to esti-
264 mate the potential impact of eddies on exchange across the shelf.

265 **4 Results**

266 **4.1 2014 Conditions**

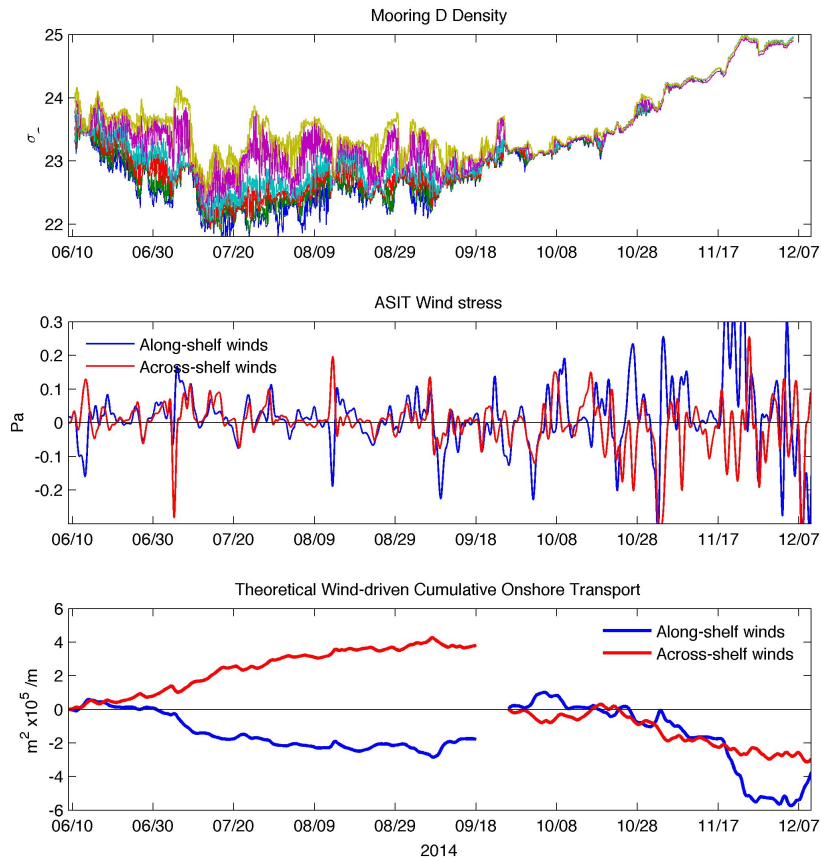
267 The ISLE study period spanned from early summer to mid-winter, 2014. Water column
268 stratification, as estimated at lander D from the top to bottom density difference (Fig. 4), in-
269 creased from June until the beginning of August due mostly to changes in temperature (not

270 shown here). On time scales of days, density and stratification varied in response to fluctu-
 271 ations in wind forcing. Westward (downwelling) winds generally resulted in reduced strati-
 272 fication (though not warming) while eastward (upwelling) winds led to increased stratification
 273 and in some cases cooling. However, large variations in density at timescales of multiple days
 274 occurred throughout the summer that were unrelated to wind events (i.e. July 10th or Sept.
 275 1st), suggesting that non-wind driven sub-tidal processes were also present during summer [*Ryp-*
 276 *ina et al.*, 2014]. After mid-September, stronger wind events are correlated with decreases in
 277 stratification and increases in water column density (Fig. 4) until the maximum density of $\sigma_\theta =$
 278 25 is reached in December.

279 Wind stress over the inner shelf south of Marthas Vineyard was predominantly to the
 280 northeast during summer [*Fewings et al.*, 2008; *Kirincich*, 2016], defined here as the period
 281 between June and September 18th when the water column is normally stratified (Fig. 4), with
 282 relatively mild wind stresses consistently between 0.05 and 0.1 PA. During winter, wind forc-
 283 ing is to the east or south east and stronger, with wind stresses generally greater than 0.1 PA
 284 [*Fewings et al.*, 2008]. However, the standard deviation of the wind stress is greater than the
 285 mean throughout the year, with variability generally occurring on short, 1-5 day time scales
 286 (Fig. 4).

290 **4.2 Background Circulation**

291 Previous model [*Wilkin*, 2006; *Ganju et al.*, 2011] and HF radar-based observational stud-
 292 ies [*Kirincich et al.*, 2013], have documented the spatial structure of the seasonally varying back-
 293 ground circulation. Onshore and adjacent to Wasque Shoals to the east of the radar coverage
 294 area, a cyclonic recirculation pattern exists that is primarily driven by tidal rectification (Fig.
 295 5). However, this signal is modified by both seasonal stratification and low-frequency winds
 296 [*Kirincich et al.*, 2013]. The size and intensity of the recirculation is larger and more intense
 297 during summer months, when winds are weak and horizontal density gradients are stronger,
 298 and weaker during winter when the density gradients are weaker. Inshore and west of this re-
 299 circulation in the northeast corner, mean surface velocities are weak until the western end of
 300 Martha's Vineyard where stronger velocities exist near gap between Martha's Vineyard and
 301 Nomans Island (Fig. 5). Offshore and south of Nomans and the southern extent of Wasque
 302 Shoal, mean velocities are along-shelf to the west. However, evidence for a westward seasonal
 303 baroclinic jet, likely associated with horizontal density gradients emanating near Nantucket Shoals
 304 [*Wilkin*, 2006], exists as the summer velocities are stronger and broader in spatial extent than

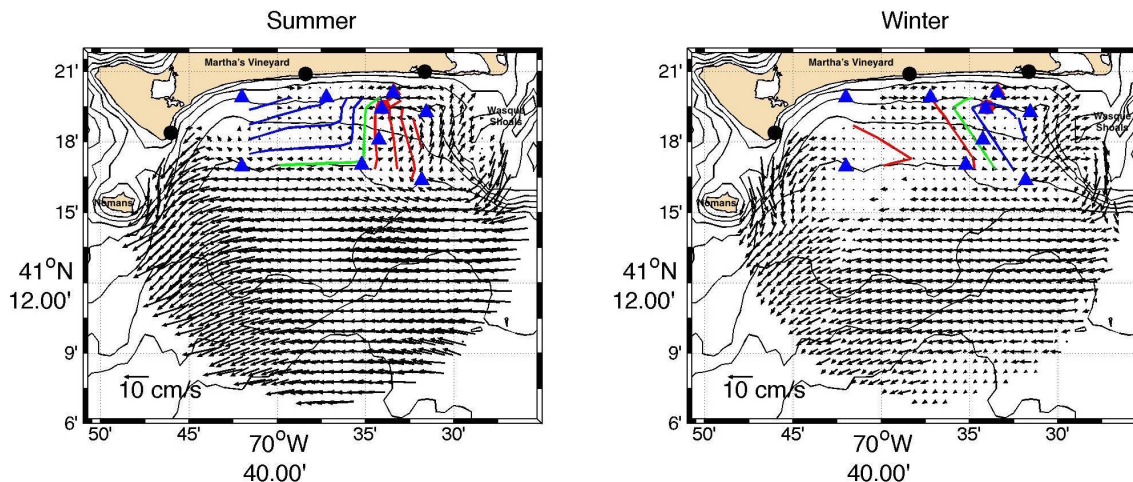


287 **Figure 4.** (top) Density at all depths (Tab. 1) observed at station D during the 2014 ISLE study period,
 288 (middle) east and north wind stress calculated from the MVCO offshore tower wind observations, and (bot-
 289 tom) integrated, wind-driven across-shelf transport in summer and winter.

305 in winter, where wide areas of reduced flow exist. This background circulation and its sea-
 306 sonal variations lead to differential transport of water masses as well as heat and salt along
 307 and across the inner shelf [Kirincich *et al.*, 2013].

313 4.3 Wind-driven Surface Layer Transport

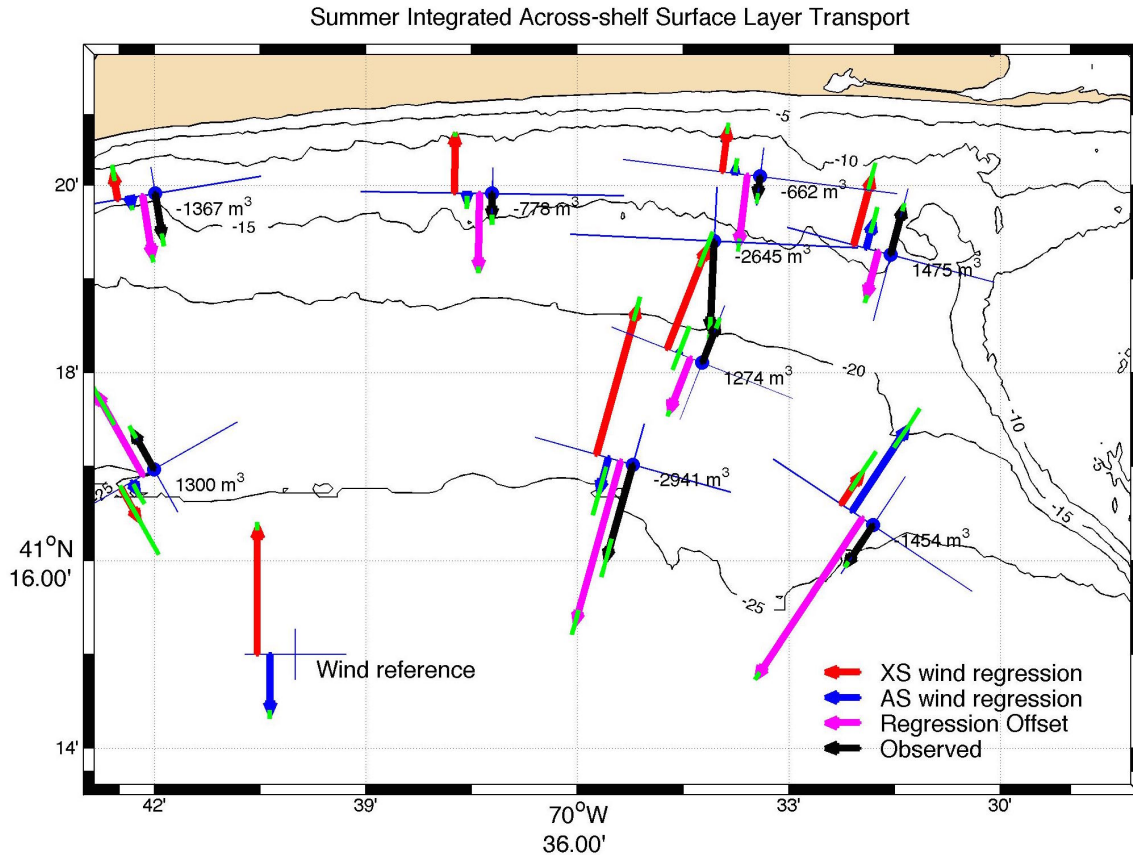
314 The orientation of the principal axis of flow across the mooring array ranged from 30
 315 to -33° relative to East (Tab. 2). Relative differences between the principal axis and the along-
 316 isobath direction was generally $\pm 5^\circ$ with the exception of stations B and F (Fig. 6), where
 317 the orientation of the principal axis crossed isobaths by up to 60° . At B, the depth-averaged
 318 flow was potentially adjusting to the southwestward orientation of the 25-m isobath that ex-



308 **Figure 5.** (left) Summer, and (right) winter time averaged surface currents within the HF radar domain.
 309 Summer is defined here by June to September 10th while winter is defined as October to mid-January. In each
 310 panel, contours of the time-averaged density anomaly at 3-m depth, based on CT observations from the
 311 moorings, is shown. The green contour denotes the zero anomaly contour while red (blue) contours denote
 312 successive 0.025 *sigma* increases (decreases) in density from the zero contour.

319 ists directly to the west of the mooring due to the presence of Nomans to the southwest. At
 320 F, the flow could be constrained by the sharp bathymetry of Wasque Shoals rising to the east
 321 of the mooring. Importantly, at all stations, the standard deviation of the along-shelf depth-
 322 averaged velocity was generally twice or more the standard deviation of the across-shelf depth-
 323 averaged velocity (Fig. 6: denoted by the relative size of the axis lengths at each mooring),
 324 suggesting that the principal axis results described here are robust.

336 To understand the potential role of surface winds in forcing across-shelf depth-dependent
 337 exchange, the observed across-shelf surface layer transport (U_{obs}) was compared to the the-
 338oretical wind-driven across-shelf transports predicted following *Lentz [2001]* and *Fewings et al.*
 339 [2008] using a multiple linear regression to characterize the components of the observed trans-
 340 port driven by the along- and across-shelf winds and the correlation between the observations
 341 and the predicted response. The theoretical transports were estimated as $U_{AS}=0.25\tau_{AS}/\rho f$,
 342 for the along-shelf component, and $U_{XS} = u^*h$ for the across-shelf component, where ρ is
 343 a reference density, f is the Coriolis parameter, τ is the wind stress, $u^* = (\tau_{XS}/|\tau_{XS}|)|\tau_{XS}|^{1/2}h/\rho$
 344 is the friction velocity, and h is the water depth (Fig. 4). The coefficient of 0.25 for the along-



326 **Figure 6.** (blue lines) The along- and across-shelf coordinate system is shown at each ISLE mooring loca-
 327 tion with the major and minor axis lengths scaled by the standard deviation of the depth-averaged velocities.
 328 (black arrows) The integrated total surface layer transport across the principal axis during summer 2014,
 329 given as m³ per day to the right of the mooring location. This observed transport can be compared to the
 330 results of the multiple linear regression between the observed transport and the along- and across-shelf winds
 331 (see text for details). The relative magnitude and direction of the integrated across-shelf surface transport
 332 due to the (red arrows) across- and (blue arrows) along-shelf winds are shown as is the (magenta arrows)
 333 integrated effect of the regression offset, as well as (green line) error bounds based on varying the principal
 334 axis $\pm 5^\circ$. An estimate of the theoretical transport for each wind component, derived from the observed winds
 335 (Fig. 4), is shown for reference.

325

Table 2. Wind-driven Across-shelf Surface Layer Transport Regressions

Mooring	Water Depth (m)	Principal Axis direction ($^{\circ}$)	Summer				Winter			
			regression offset ^a	Wind		regression offset ^a	Wind		r	
				AS	XS	r		AS	XS	r
A	15	-9.3	-0.02	0.25	0.36	0.42	0.03	0.01	0.32	0.62
B	25	29.5	0.03	1.24	-0.23	0.64	0.01	0.36	0.21	0.60
C	15	-0.9	-0.03	0.17	0.90	0.67	0.02	-0.08	0.63	0.89
D	25	-15.6	-0.06	0.45	1.59	0.71	0.04	-0.26	0.61	0.75
E	15	-14.9	-0.02	-0.36	1.31	0.80	-0.02	-0.12	0.43	0.88
F	25	-33.5	-0.07	-1.05	0.84	0.67	0.03	-0.54	0.48	0.81
G	12	-7.0	-0.02	-0.11	0.93	0.82	0.02	-0.14	0.55	0.87
H	16	-2.7					0.02	-0.12	0.63	0.82
I	21	-21.5	-0.02	-0.05	1.59	0.80	-0.01	-0.39	0.58	0.84

^a in m^2/s per along-shelf m

345 shelf Ekman transport has been previously found to represent the response of the inner-shelf
 346 at these water depths to along-shelf wind forcing [Lentz, 2001; Kirincich *et al.*, 2005].

347 Across the domain, the predicted transport based on the regression was generally sig-
 348 nificantly correlated with the observed transport, accounting for 42-64% of the observed trans-
 349 port variance in summer, ignoring mooring A as an outlier, and 36-81% of the transport vari-
 350 ance in winter. The regression coefficients themselves serve as indicators of how responsive
 351 U_{obs} was to each component of the wind. Regression coefficients varied with water depth as
 352 is expected from the results of [Lentz, 2001], but also varied with along-shelf distance, poten-
 353 tially due to the increase in stratification, although only the mean effect of stratification is con-
 354 sidered below. During winter, across-shelf winds made the dominant contribution to the re-
 355 gression at all moorings except stations B and F, where the along- and across-shelf compo-
 356 nents were roughly equal in magnitude, although the along-shelf component at F still had the
 357 opposite sign as what would be expected via Ekman transport (Tab. 2). At all stations, the re-
 358 gression coefficient magnitudes were less during winter than what was found during summer.

359 During summer, the regressions at moorings C, E, and G onshore favored forcing from
 360 the across-shelf winds, as across-shelf wind regression coefficients were 0.9 to 1.3 while along-

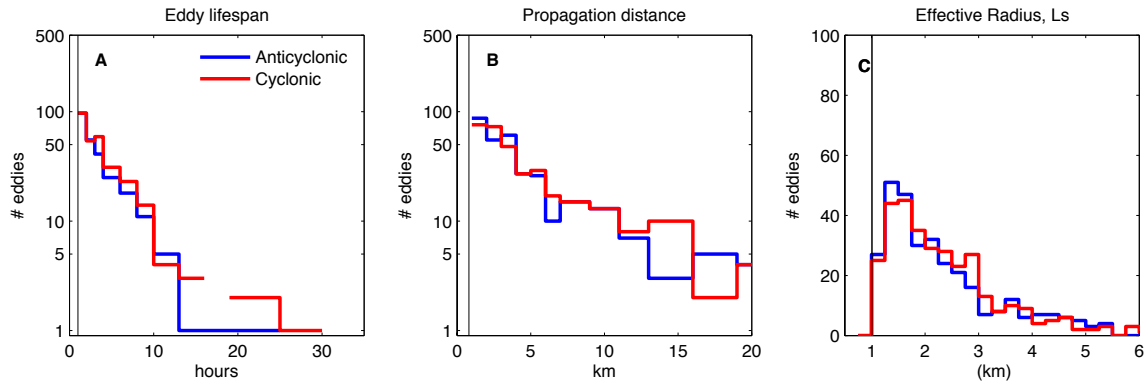
361 shelf wind regression coefficients were greatly reduced (Tab. 2). At D and I offshore, the sum-
 362 mer regressions also favored forcing from the across-shelf winds, with regression coefficients
 363 near 1.6 while along-shelf wind regression coefficients were small in comparison (Tab. 2). The
 364 lower correlation and regressions seen at A (Tab. 2) were due in part to its location outside
 365 of the radar domain that required a different surface extrapolation technique. Estimating the
 366 transport calculation using the non-radar extrapolation at station G (not shown here) gives re-
 367 gression correlations that are 0.2 lower than that shown in Tab. 2. At stations B and F, the sig-
 368 nificant rotation of the principal axis caused significant deviations in the wind-driven trans-
 369 port regressions. At B, the dominant winds to the northeast aligned with the along-shelf com-
 370 ponent, leading to a regression that favored the along-shelf winds with a regression magnitude
 371 of 1.24. At F, the response to the along and across-shelf winds were more evenly matched in
 372 amplitude, however the along-shelf regression coefficient has the opposite sign as what would
 373 be consistent with Ekman dynamics. This peculiar result will be discussed later. While these
 374 results show that theoretical estimates are indeed a reasonable predictor of the observed trans-
 375 port, especially during summer, the spatial variations in the regression values are as great as
 376 50% of the values themselves, suggesting that strong gradients in wind-driven circulation can
 377 exist on spatial scales of kilometers.

378 The regression offsets representative the mean or integrated effect of the non-wind driven
 379 transport observed at the mooring location. In general, the offset is small relative to the size
 380 of the variations in the surface transport driven by the wind. For example, the standard devi-
 381 ation of the theoretical along or across-shelf transport driven by either wind component is $O(0.1)$
 382 $\text{m}^3 \text{s}^{-1}$ per along shelf m, while the mean of the non-wind driven transports are less than 0.03
 383 $\text{m}^3 \text{s}^{-1}$, except for at stations D and F during summer. Notably, the mean transports are di-
 384 rected offshore in the summer and onshore in the winter. While the magnitudes of the regres-
 385 sion offsets are small, they can have a sizable impact in the integrated depth-dependent trans-
 386 port observed at the moorings due to the fluctuating nature of the winds, as shown below.

387 **4.4 Coherent Eddies**

388 ***4.4.1 Occurrence and Distribution***

389 Between June 10th and December 5th, 2014, 635 eddies were identified within the foot-
 390 print of the HF radar system during the mooring deployment. In general, statistics of the ed-
 391 dies identified (Fig. 7) were similar for both anticyclonic and cyclonic eddies. Eddies tended



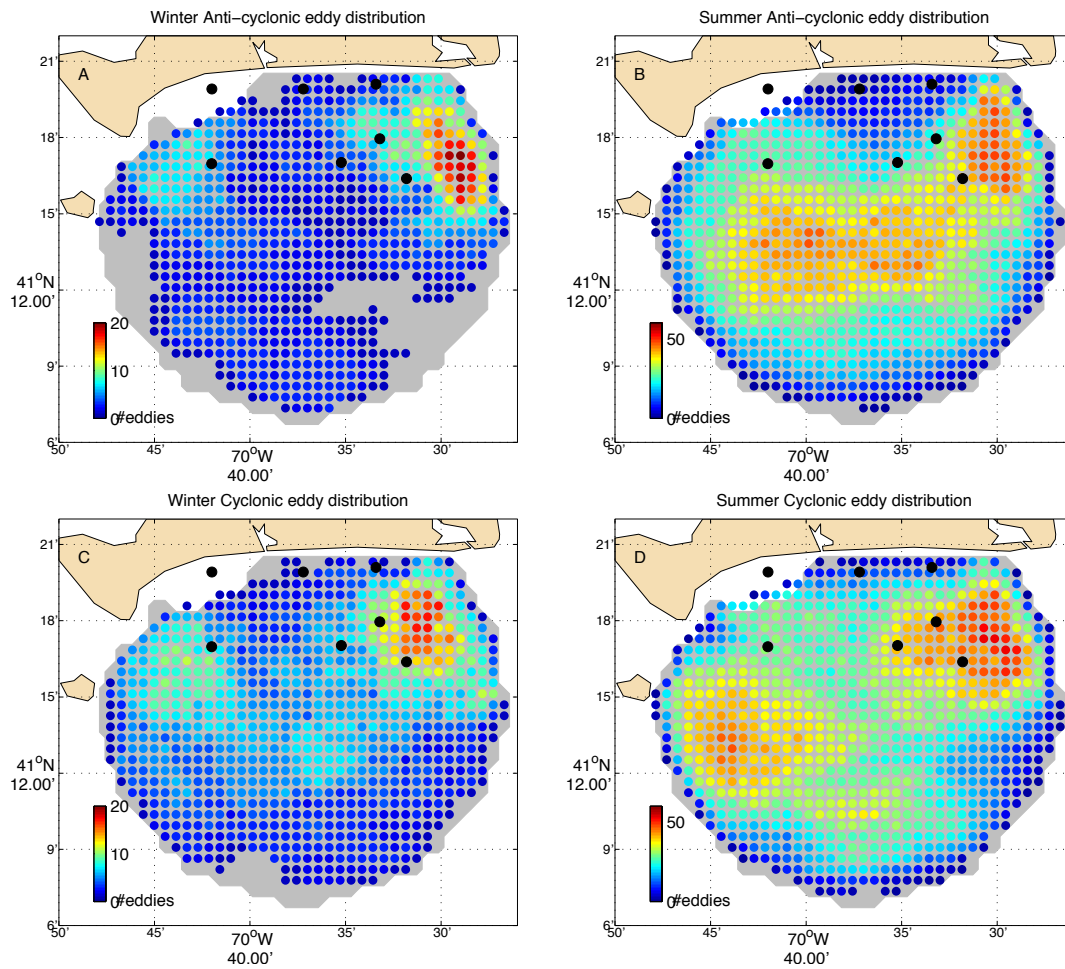
396 **Figure 7.** Eddy statistics including (A) eddy lifespan, (B) propagation distance, and (C) effective radius –
 397 as the radius of a circle having an area to that of the eddy.

392 to move less than 5 km from their starting point over their relatively short, 2-10 hour, lifes-
 393 pans (Fig. 7). The mean effective radius of the eddies had a peak at 1.5 km with a slow rolloff
 394 to radii of 3 to 6 km (Fig. 7). Thus, most eddies do not translate horizontally more than their
 395 effective diameter.

398 Eddies are more often found in summer than winter, and the area adjacent to Wasque
 399 Shoals (Fig. 8) dominates eddy activity in both seasons. Examining the spatial distributions
 400 of eddies during summer, eddy occurrences can be organized into approximately six ‘hot spots’
 401 of eddy activity, classified by both the location of the eddy and its rotational direction. An-
 402 ticyclonic eddies were most often found within the (1) northeast corner adjacent to the Wasque
 403 Shoal (Fig. 8), but also within a (2) broad area in the middle of the domain, located approx-
 404 imately inshore of the main axis of the along-shelf coastal current present during summer (i.e.
 405 Fig. 1). A notable portion of this broad area of anticyclonic eddies is adjacent to the (3) west-
 406 ern edge, centered at $41^{\circ} 13' N$, $70^{\circ} 44' W$. Cyclonic eddies were found within an expanded
 407 portion of the (4) northeast corner as well along the (5) western edge and (6) offshore of 41°
 408 $12' N$, south of the main axis of the along-shelf coastal current during summer (Fig. 1).

412 **4.4.2 Characteristic Eddy Types**

413 The six eddy types, defined above and in Tab. 3, account for 529 of the 634 eddies iden-
 414 tified. Each represent a characteristic flow field of the study area as can be seen in a compos-
 415 ite average of the velocity fields during each eddy type (Fig. 9). Importantly, while averag-
 416 ing in geographic coordinates has the potential to smear out the spatial structure of both the



409 **Figure 8.** Eddy density, defined as the number of eddies seen at a grid point for (top) anti-cyclonic and
 410 (bottom) cyclonic eddies during (left) winter – September 18th to December 5th, 2014 – and (right) summer,
 411 June 9th to September 18th, 2014. Note the range of the color bar is different for winter and summer.

417 eddy and the surrounding flow field, tests building composite views within an eddy-centric ref-
 418 erence frame gave a qualitatively similar result as that shown here for the circulation of the
 419 eddies themselves, but had the larger negative effect of biasing the far-field flow structures.

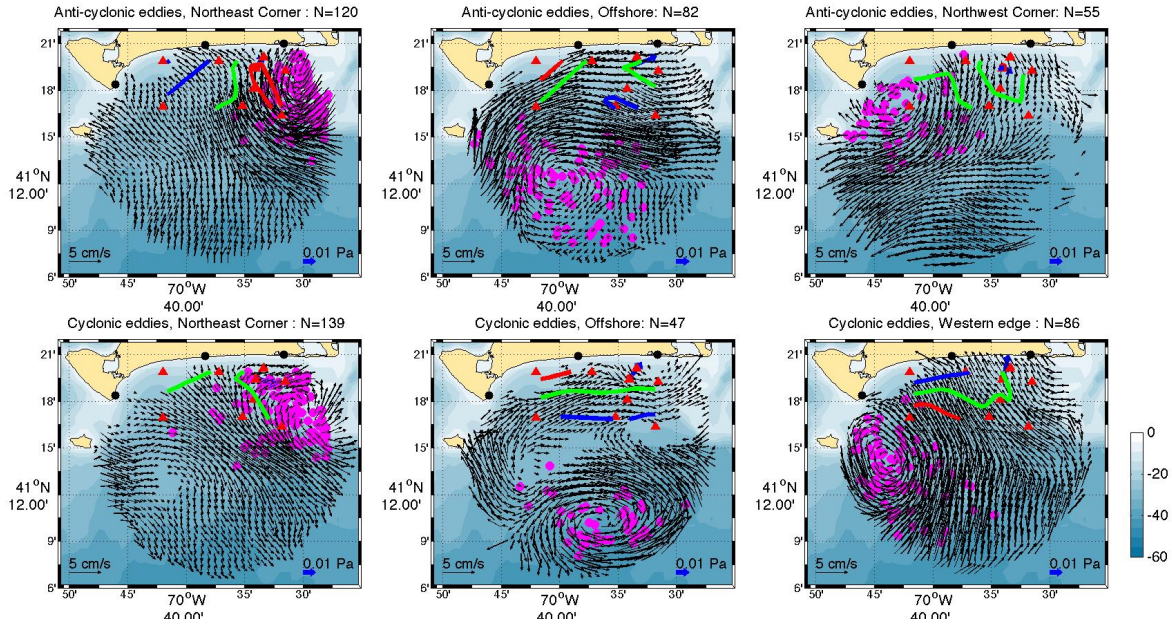
420 Anti-cyclonic and cyclonic eddies in the northeast corner (Fig. 9, left), encompassing
 421 those previously described by *Kirincich* [2016], are the most numerous but generally have smaller
 422 effective radii and shorter lifespans relative to those identified elsewhere within the domain
 423 (Tab. 3). The dominant non-tidal flow present at scales larger than the eddy is strong and to
 424 the northwest (southeast) for anti-cyclonic (cyclonic) eddies, suggesting that the eddies them-
 425 selves are wedged between this cross-isobath flow and Wasque Shoals to the east. Examin-
 426 ing the mean composite near-surface (3-m) density anomaly, formed by removing the spatial
 427 structure of the monthly mean density spatial anomaly (Fig. 5) from the spatial anomaly of
 428 density during all eddies of each characteristic type, the composite eddy anomaly was near zero
 429 for cyclonic eddies within the northeast corner but had a $\sigma=0.04$ difference across the west-
 430 ern side of the composite anti-cyclonic eddy, with denser waters located within the eddy core.

431 Eddies along the western edge (Fig. 9, right) appear to interact strongly with both the
 432 western edge of Martha's Vineyard and Nomans to the south. Cyclonic eddies of this type are
 433 tightly distributed just east of Nomans and tend to occur during winds to the north with strong
 434 onshore surface currents throughout the domain east of the eddy. Anti-cyclonic eddies in the
 435 northwest corner are more diffuse in location, have relatively small effective radii, weak den-
 436 sity anomaly gradients, and are associated with strong surface flow offshore to the southwest,
 437 but relatively weak winds.

438 Eddies found offshore (Fig. 9, center) are the largest of all the eddies observed (Tab. 3),
 439 for both rotational directions. Average winds were strong and to the northeast during occur-
 440 rences of offshore eddies, and surface currents onshore at the moorings were to the east and
 441 consistent with the observed density anomaly gradients (see below). Offshore, the compos-
 442 ite flow suggests an along-shelf jet exists onshore of both eddy types. However, the locations
 443 of the anti-cyclonic offshore eddies are fairly diffuse to the south, potentially influencing the
 444 composite view seen.

456 **4.4.3 Eddy Depths**

457 Estimated depths for most eddy types were similar, to within the standard error of the
 458 mean eddy depth, particularly at 1-1.5 radii away from the eddy center. Inside of 1 radii from



446 **Figure 9.** Composite surface currents present during each of the 6 characteristic eddy types (Tab. 3). For
 447 each panel, the time-averaged surface currents present over the life of each eddy are averaged for all eddies
 448 within each eddy type (Tab. 3). Only eddy averaged mean currents that are larger in magnitude than the stan-
 449 dard error are shown. Additionally, the mean location of the center of each eddy (magenta dot) within the
 450 characteristic type are shown to illustrate the potential smearing of the composite surface current field due
 451 to the spatial variability of the eddy locations themselves. Superimposed on the velocity fields are the eddy
 452 averaged density anomaly contours at 3-m depth (with a contour interval of $\sigma_t=0.02$) formed by removing the
 453 seasonally varying background density structure shown in Fig. 5 from the instantaneous densities estimated at
 454 the moorings. The composite-averaged wind stress, observed at the offshore tower near station H (Fig. 1) is
 455 shown at the tower location (thick blue arrow).

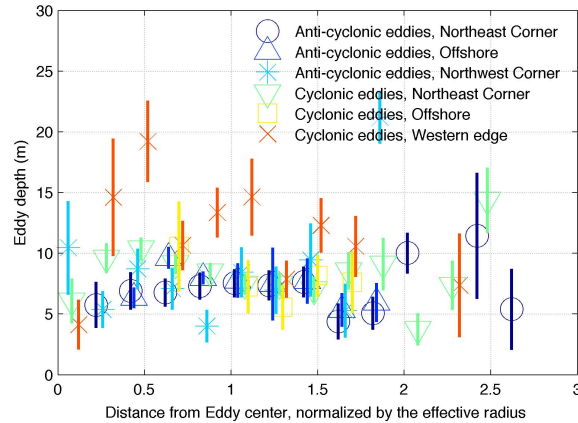
445

Table 3. Characteristic Eddy Type Statistics

Rotation	Location definition	# Eddies	Effective Radius (km)		# Eddies w/depths	Eddy Depth (m)	
			Mean	Std Dev		Mean	Std. Dev.
Northeast Corner							
Cyclonic	North of 41° 15', East of 70° 36'	139	2.1	0.8	84	8.4	0.5
Anticyclonic	North of 41° 15', East of 70° 33'	120	1.9	0.6	55	6.8	0.7
Western Border							
Cyclonic	South of 41° 17', West of 70° 40'	86	2.7	1.2	18	13.2	1.4
Anticyclonic	North of 41° 15', West of 70° 37'	55	2.3	1.1	26	6.8	1.3
Offshore							
Cyclonic	South of 41° 12', East of 70° 42'	47	2.7	1.2	5	9.1	2.4
Anticyclonic	South of 41° 15', West of 70° 33'	82	2.9	1.2	12	8.9	1.6

459 the center, cyclonic eddies found along the western edge had the deepest depths, at 10-18 m
 460 0.5-1 radii away from the center, the approximate sill depth between the western edge of Martha's
 461 Vineyard and the Nomans Island offshore to the south. Cyclonic eddies in the northeast cor-
 462 ner also had slightly greater eddy depths than the remainder of the eddy types, with values of
 463 10-12 m at 0.25-0.5 radii from the eddy center, similar to the shoal depth directly to the east.
 464 Due to the detection method used, eddy depths are likely to be biased low when detected at
 465 the center of the eddy where flow is the most quiescent and velocity errors might lead to in-
 466 creased veering with depth. This can be seen in Fig. 10, as most eddies have smaller depths
 467 and higher uncertainties at small distances from the eddy center.

468 In general, depth estimates were possible at less than half of the eddies for most eddy
 469 types (Tab. 3). While depths were available for 60% of the cyclonic eddies in the northeast
 470 corner due to their proximity to the moorings, only 10% of the cyclonic eddies offshore were
 471 seen at the moorings. While offshore eddy depths were between 5 and 10 m (Fig. 10), it should
 472 be noted that only the largest offshore eddies were observed at the moorings and most of depth
 473 estimates were at edge the of eddies due to relative location of eddies and moorings.

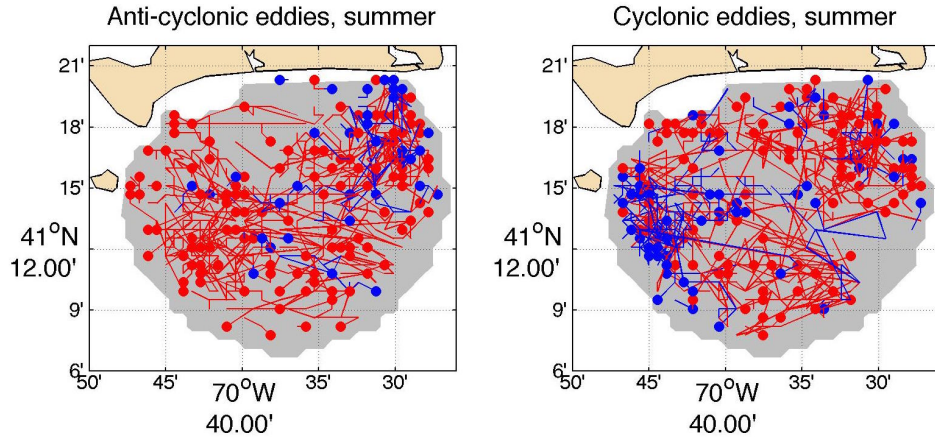


474 **Figure 10.** Mean and one standard error for the eddy depth for each eddy type with distance away from the
 475 eddy center.

476 **4.4.4 Eddy Drivers**

477 An integrated look at the coupled occurrence of potential forcing conditions and eddies
 478 allows insight into the types of conditions that are most favorable for eddy generation. In this
 479 context, the role of the tide or wind-forced currents and the local bathymetry as well as in-
 480 stabilities of the across-shelf density gradients and/or baroclinic currents present are examined
 481 below.

482 **Winds:** While no clear relationship to wind speed exists for eddy formation, as was found by
 483 *Kirincich* [2016] in the northeast corner, wind direction does play a role in determining when
 484 and where eddies will normally form throughout the study area. Cyclonic eddies appear to form
 485 along the western boundary predominately during winds to the northwest (Fig. 11, right panel,
 486 blue dots), where the larger flow field around the eddy is strong and onshore directed at the
 487 surface (Fig. 9). In contrast, anti-cyclonic eddies forming during northwestward winds are most
 488 often found in the northeast corner (Fig. 11, left panel, blue dots). Comparing the compos-
 489 ite eddy structures with the direction of the wind and surface flows for these eddy types sug-
 490 gests that eddies during northwestward winds might form predominantly due to blocking of
 491 the wind-driven flow by local topography. During winds to the northeast, both eddy types are
 492 more widely distributed, with the exception of a local minimum in eddy activity along a north-
 493 westward line across the domain (Fig. 11). In many of the eddy types, the strongest compos-
 494 ite velocities are found along this line, suggesting this is the general position of the along-shelf
 495 coastal current described by *Wilkin* [2006] during eddy generation (Fig. 9). However, winds

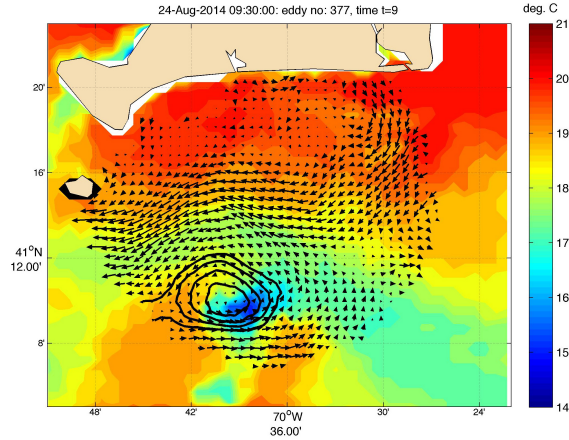


498 **Figure 11.** The starting location and total track line of the center of all anti-cyclonic (left) and cyclonic
 499 (right) eddies present during summer. Eddy tracks are colored by the direction of the wind forcing during the
 500 time of the eddy, where red tracks occur during times of winds to the northeast and blue tracks occur during
 501 times of winds to the northwest.

496 to the northeast are the dominant wind direction during summer and thus some of the processes
 497 leading to the distributions seen for northeastward winds might not be due to the wind itself.

502 **Tides:** A fraction of the eddies in the northeast corner appear to be linked to the phase of the
 503 M_2 tide as eddies of both rotational types are more likely to occur at max flood or ebb than
 504 other phases of the local tide. As illustrated by *Kirincich* [2016], this is of interest as simple
 505 vortex stretching of tidal flows [*Robinson*, 1981] does not account for the generation of cy-
 506 clonic and anticyclonic eddies on both ebb and flood tide conditions, but suggests a more com-
 507 plex spatial structure of tidal phase. However, eddies in the northeast corner do occur at all
 508 phases of the tide, suggesting that a large portion of the composite structure seen in (Fig. 9)
 509 might be due to non-tidal effects such as the wind effects described above. Along the west-
 510 ern boundary, in proximity to stronger tidal flows between Martha's Vineyard and Nomans,
 511 cyclonic eddies occur twice as often during times of slack water as observed at mooring B,
 512 in contrast to the link between maximum tidal flows and eddies in the northeast corner.

513 **Horizontal Density Gradients:** Near-surface gradients in density within the composite eddy
 514 averages (Fig. 9) are generally weak except for during anti-cyclonic eddies in the northeast
 515 corner and offshore eddies. For anti-cyclonic eddies in the northeast corner, composite sur-
 516 face velocities in the eastern part of the study area are onshore and, despite appearing to be



528 **Figure 12.** Example of a cyclonic offshore eddy with coincident and clear SST imagery found on
 529 09:30 GMT, August 24th, 2014. Eddy streamlines (black lines) are shown over the residual (with both
 530 the tide and the monthly mean removed) surface current field. The SST imagery was downloaded from
 531 www.maracoos.org and reprocessed to mask for land, clouds, and correct for geo-rectification errors.

517 along lines of constant density anomaly (Fig. 9), against the direction of a thermal wind shear
 518 between the horizontal density gradient and the velocity field, assuming weak flow at the bot-
 519 tom. For the eddies found offshore, the flow located in and around the mooring locations ap-
 520 pears to be along lines of constant density anomaly (Fig. 9), and has a direction consistent with
 521 a thermal wind balance. With a composite 0.04 kg m^{-3} density change between the 15-m and
 522 25-m moorings (a 5 km separation), the thermal wind velocity would be $\sim 2 \text{ cm/s}$ at the sur-
 523 face, similar to the observed velocity magnitudes. Farther offshore at the locations of the off-
 524 shore eddies themselves, anecdotal evidence from the small number of eddies with concur-
 525 rent cloud-free SST imagery suggests that density gradients or baroclinic processes are a po-
 526 tential driver for these eddy types. For example as shown in Fig. 12, a cyclonic eddy exists
 527 along the offshore edge of a plume of cooler waters meandering through the study area.

532 **4.5 Transport Comparisons**

533 The relative importance of wind-driven transport, eddy-driven transport, and the back-
 534 ground spatial variability on exchange across the inner shelf can be quantified by integrating
 535 the volume of water predicted to move across the 25-m isobath – represented here in units of
 536 m^3 per along-shelf m, or m^2 , per day – due to each process. These estimates are confined to

537 the summer stratified period, June 9th through September 18th, defined based on the break-
 538 down of stratification seen thereafter (Fig. 4),

539 **4.5.1 Wind-Driven Depth-Dependent Transport**

540 The observed across- and along-shelf winds have competing influence on the direction
 541 and magnitude of exchange across the shelf (Fig. 4). The integrated theoretical across-shelf
 542 transport due to the across-shelf winds would result in 3762 ± 120 m² per day directed onshore,
 543 while the integrated effect of the along-shelf winds would provide 1760 ± 120 m² per day of
 544 transport directed offshore (Fig. 6). Uncertainty estimates for both wind-driven transports were
 545 assessed by assuming a potential bias in the wind speed of up to ± 0.1 m/s and computing the
 546 subsequent range of wind-driven transports.

547 For the wind-driven across-shelf surface layer transport, the regression coefficients shown
 548 in Tab. 2 were used to predict the total transport realized at each mooring due to the along-
 549 and across-shelf winds. Using this approach, the potential effect of the winds are integrated
 550 over the full summer for all stations, even though the observations at stations D, H, E, and I
 551 are shorter in length (Tab. 1). Numerous sources of error exist in the transport estimates that
 552 lead to uncertainty in the summer integrated transport estimates. The potential range of un-
 553 certainty present was estimated by varying the orientation of the principal axis of flow, a crit-
 554 ical component of the across-shelf transport calculation, at all moorings by $\pm 5^\circ$ and re-calculating
 555 the regression results and the integrated transports [following *Fewings and Lentz, 2011*].

556 In general, the integrated surface layer transport due to along-shelf and across-shelf winds
 557 at the moorings also have competing influences (Fig. 6), however, large differences exist in
 558 the magnitude of both components between the mooring locations. Offshore, both the across-
 559 and along-shelf wind-driven transport change sign from B to F, or west to east. As the local
 560 winds are rotated into along and across-shelf coordinate system at each location, a portion of
 561 the difference was due to the difference principal axis orientation. Yet, the differences in wind-
 562 driven exchange between stations D and F, with across-shelf wind-driven exchange being 4.5
 563 times larger at D and along-shelf wind-driven exchange being the opposite sign at F are more
 564 significant than what the difference in orientation would provide. Onshore at stations A, C,
 565 G, and E, the across-shelf wind-driven exchange generally increases from 825 ± 228 to 2070 ± 423
 566 m² per day directed onshore from west to east, while the along-shelf wind-driven exchange

567 was weak in comparison, varying from $\sim 300 \pm 100 \text{ m}^2$ per day directed offshore at A and C
 568 to $200\text{-}800 \text{ m}^2$ per day directed onshore at G and E.

569 The observed transport (Fig. 6: black arrows), the time integral of U_{obs} , within the sur-
 570 face layer over the summer, ranged from 1300 m^2 onshore at B to 1300 m^2 offshore at F with
 571 small uncertainties. Onshore, observed transports were up to $\pm 1300 \text{ m}^2$ per day but highly
 572 variable both in magnitude and direction. It is important to note that stations D, H, E, and I,
 573 the observed transport is estimated over a shorter time period than the wind-driven transport,
 574 due to the shorter record lengths, potentially contributing to the larger variability seen at these
 575 stations. By definition, the residual transport (Fig. 6: magenta arrows) is the difference between
 576 the combination of the wind-driven transports, based on the regressions between the wind and
 577 the surface layer transport, and the observed transport. Thus, the residual can be thought of
 578 as the integrated effect of all other processes that also drive depth-dependent exchange. At all
 579 stations except B, the residual was directed offshore, but the magnitude varied dramatically,
 580 up to 5500 m^2 at F.

581 **4.5.2 Eddy Transport**

582 Following *Kirincich* [2016], tracking particles that start within the eddy over the lifes-
 583 pan of the eddy serves as an estimate of how eddies – defined solely by their stream function
 584 – are able to trap and move water parcels in addition to that linked directly to depth-dependent
 585 wind forcing. Focusing on eddies that were seen near the 25-m isobath, as direct estimates of
 586 their vertical extent observed at stations B, D, F, or I can be used to estimate the volume trans-
 587 port, the potential uncertainty of the effects of eddies on exchange was assessed by varying
 588 the eddy depths by the standard deviation of eddy depths for each eddy type (Fig. 10) and es-
 589 timating the range of transports that would result. Within the domain, eddies generally moved
 590 offshore thus the eddy mean, or translational, effect transports volume offshore, with cyclonic
 591 and anti-cyclonic eddies contributing roughly equal amounts (Tab. 4). Integrated over the sum-
 592 mer, the total translational effect of the eddies alone ($331 \pm 79 \text{ m}^2$ directed offshore) accounted
 593 for exchange equal to 17% of the combined theoretical wind-driven depth-dependent exchange
 594 ($2002 \pm 240 \text{ m}^2$ directed onshore) but in the opposite direction. However, taking each of the
 595 mooring-based wind-driven results as an estimate of the surface layer transport across the 15
 596 or 25-m isobaths, the mean across-shelf transport due to the winds is 799 ± 211 and 999 ± 650
 597 m^3 per along-shelf m per day directed onshore for both the 15 and 25-m isobaths. Thus, in
 598 this context, the eddy driven exchange is more than 1/3 of the wind-driven exchange.

613

Table 4. Summer Daily-averaged Across-shelf Transport^a

Coherent Eddies						
Eddy type	Eddy		Line			
	Mean	Relative	Mean	Relative		
Anti-cyclonic	-155±36	546±365	~0	1413±910		
Cyclonic	-161±43	556±375	~0	1443±942		
Total effects across 25-m isobath						
	Wind		Eddy		Background	
	Mean	Relative	Mean	Relative	Mean	Relative
	997±650 ^b	1757±1300 ^b	-316±79	1101±740	642±122	3433±853

^a in m³ per along-shelf m, or m², per day^b see discussion for calculation details

599

600

601

602

603

604

605

606

607

608

609

610

611

612

Given that most eddies don't translate far relative to their diameter, the ability of an eddy to move a particle of water from one side to another, defined here as its relative transport over its lifespan, is potentially more important to exchange across the shelf than the simple translation of the eddy. During summer, this relative effect contributed an additional $\sim 550 \pm 370$ m² per day of volume transport for both rotational directions (Tab. 4). As shown by *Kirinich* [2016], coherent eddies in the study area generally exist as local minima of eddy kinetic energy within the flow field. Thus, how much of the total relative exchange observed occurs within the defined eddy itself, as opposed to outside the eddy, is an important aspect of this calculation. Advecting particles starting along an along-shelf line centered at the 25-m isobath over the lifespan of each eddy allows an estimate of how much of the rotational effect caused by the eddy was located inside the eddy. The relative volume transport of the line particles was almost three times the relative transport of the in-eddy particles for both eddy types (Tab. 4), suggesting that the eddy itself accounts for a fraction of the relative volume exchange due to the conditions that lead to eddy formation.

614

4.5.3 Background Transport

615

616

The spatial mean cumulative transport of the background flow field (Fig. 5) can be similarly estimated by integrating the monthly averaged velocity structure, which was removed

617 from the residual velocities used to estimate depth-dependent transport and eddy transport, over
618 the summer period. Despite potential evidence that this flow structure might be uniform with
619 depth [*Ganju et al.*, 2011; *Kirincich et al.*, 2013], a mean surface layer thickness of 10 m is
620 assumed for consistency with the above estimates. Applied to an along-shelf line centered at
621 the 25-m isobath, the mean and relative exchange due to the background circulation is 642 ± 122
622 and $3433 \pm 853 \text{ m}^2 \text{ s}^{-1}$ per day (Tab. 4). Uncertainty estimates for the background transport
623 were made by propagating the standard error of the mean and anomaly fields.

624 **5 Discussion**

625 **5.1 Depth Dependent Exchange Variability**

626 The across-shelf surface layer transport is used here as an indicator of how variable in-
627 ner shelf circulation can be within the study area. The combined use of HF radar surface cur-
628 rents and moored ADCP results represents the best estimate of the true surface layer trans-
629 port because of its ability to capture the near surface shear. Across the mooring array, the sur-
630 face layer transport varied dramatically, up to 100% of the theoretical value based on the wind
631 stress, likely because of variability in wind- and non-wind driven transport processes. Both
632 are discussed further here.

633 Establishing the local coordinate system was critical to most aspects of the analysis, hence
634 its use in estimating the transport uncertainties. While rotating observed velocities into an along
635 and across-shelf coordinate system based on the principal axis of the depth-averaged flow has
636 been utilized for some time [e.g. *Kundu and Allen*, 1976] to understand the effects of the wind
637 on across-shelf dynamics relative to the more dominant along-shelf dynamics, in context of
638 a larger number of mooring locations with variable bathymetric conditions, it is unclear if a
639 more appropriate definition for along-shelf is necessary. In general, small rotations of the prin-
640 cipal axis have large results, particularly at the offshore stations. Offshore, the relative angle
641 between the principal axis and the dominant wind direction varied by up to 50° , and thus was
642 a factor in determining the regression magnitude and direction of the wind driven surface layer
643 transport. However, estimating the regression between the surface layer transport and wind-
644 driven transports on a non-rotated, east and north coordinate system, there are still differences
645 in the regression coefficients of up to 50% over relatively small spatial scales (not shown here).
646 Thus, the definition of along-shelf is not the only reason for the differences seen.

647 Independent of the coordinate system itself, differences from the predicted transport are
 648 likely due to either variations in stratification, which would drive a different magnitude response
 649 in the surface layer, or differences in the winds themselves. While the spatial variability of the
 650 wind was not measured at mooring sites other than the tower near station H, comparing wind
 651 observations from station H to land-based sensors up to 10-15 km away found only small dif-
 652 ferences during times of onshore winds which include the dominant wind direction out of the
 653 southwest. However, there are notable spatial variations in the mean stratification that partially
 654 explain the spatial trends in the response to the wind. The time-mean top to bottom stratifi-
 655 cation decreases from 0.04 to 0.028 kg m⁻³ /m moving from west to east along the 15 m iso-
 656 bath along with the increase in the across-shelf wind regression coefficient (Tab. 2). Offshore
 657 stations have mean stratifications of 0.045-0.045 kg m⁻³ /m except F, which at 0.038 kg m⁻³
 658 /m is more similar to the 15 m sites in stratification magnitude and regression coefficients. As
 659 discussed in *Lentz and Fewings* [2012], decreased stratification at a given water depth would
 660 favor a stronger response to the across-shelf wind forcing than that seen for the along-shelf
 661 winds. In contrast, the along-shelf wind-driven responses at F and E were not consistent with
 662 Ekman transport. The observed response is more likely related to the onshore-offshore move-
 663 ment and/or veering of the along-shelf coastal current, such as that shown in Fig. 9. As de-
 664 scribed by *Kirincich* [2016], wind forcing of the ocean surface could translate an along-shelf
 665 current across the shelf, leading to variations that are correlated with the wind itself.

666 **5.2 The Implications of Eddies**

667 As coherent eddies appear to be an important component of the lateral exchange observed
 668 south of Martha's Vineyard, understanding what types of processes generate eddies is criti-
 669 cal to assessing how important eddy driven exchange might be in other coastal systems. A frac-
 670 tion of the eddies occurring within the northeast corner were generally linked to the tide, in
 671 that many occur on particular phases of the M₂ tide, but whether an eddy is found within the
 672 northeast corner appears to also depend on wind direction. The spatial extent of the eddy hot
 673 spot within the northeast corner is not significantly different between winter and summer, and
 674 is similar in along and across-shelf extent to the offshore extent of the shoals itself. Thus, de-
 675 spite differences in wind forcing and stratification which clearly affect the total numbers of
 676 eddies found, the area of the inner shelf subject to additional small-scale eddy fluxes due to
 677 the presence of the shoals is limited to an area not larger in extent than that of the shoals it-
 678 self.

679 To the west, the occurrence of eddies along the western boundary is less often linked
680 to the phase of the tide in the area, but more to the direction of the wind and the dominant
681 along-shelf flow, suggesting that flow around the topography is important. However, as the lo-
682 cation of the eddy hot spot along the western edge changes from winter to summer, stratifi-
683 cation is likely to also be a factor. Inshore, where the eddies crossed the locations of multi-
684 ple moorings, eddies were seen to form both within an existing horizontal density structure,
685 such that the eddy streamlines align with near-surface isopycnals, as well as form across isopy-
686 cnals and advect or deform the existing horizontal density structure. For most of the eddy types,
687 wind direction might control the eddy formation as wind direction appears to control the larger
688 scale flow field and its interaction with the existing bathymetric barriers. In contrast, eddies
689 found offshore during times of good SST imagery consistently had eddy streamlines aligned
690 with isotherms (Fig. 12). If representative of the bulk of offshore eddies, this suggests that di-
691 rect wind forcing was not the dominant driver of eddy activity offshore.

692 **5.3 Consistency of Transport Estimates**

693 The depth-dependent wind-driven, eddy, and background transports are each assessments
694 of different processes that cause lateral variations in circulation and the exchange across the
695 inner shelf. The general direction of the observed surface layer transport over the mooring ar-
696 ray (Fig. 6) is offshore but with transport magnitudes, integrated over the summer, that are smaller
697 than the volume of the inner shelf itself. This is in contrast to stronger upwelling regions such
698 as the Oregon or California coast where the volume of the inner shelf is generally smaller and
699 the integrated surface layer transport over the summer upwelling season is larger. Using typ-
700 ical values for the inner shelf width and the observed across-shelf transport from inner shelf
701 moorings [Kirincich *et al.*, 2005], the Oregon shelf realizes wind-driven exchange equal to 6-
702 10 times the volume of the inner shelf over the summer upwelling season. Spatial variations
703 of the response to wind forcing seen in the depth-dependent surface layer transport over the
704 Martha's Vineyard inner shelf are significant (Fig. 6), adding 1-2 additional inner-shelf vol-
705 umes of exchange in the form of large-scale horizontal stirring.

706 The spatial structure of the background flow (Fig. 5, Tab. 4) reveals that a significant
707 amount of across-shelf transport can be driven by lateral variability independent of the wind
708 or eddy activity. While the exact meaning of the relative exchange for wind and eddy-driven
709 processes and its impact has not been quantified, the background circulation that causes the
710 large-scale relative exchange is not, and has been shown to lead to real fluxes of heat across

711 the shelf [Wilkin, 2006; Fewings and Lentz, 2011; Kirincich *et al.*, 2013]. However, this exchange
712 is driven by tidal rectification, in contrast to the wind and a number of the characteristic eddy-
713 driven exchanges. The coherent eddies identified using the eddy-finding methodology are small
714 in spatial scale, short-lived in time, and generally uncorrelated with the wind and thus repre-
715 sent additional transport that is not accounted for in typical mooring-based estimates of ex-
716 change.

717 It is possible that a portion of the residual exchange seen at the moorings, which gener-
718 ally counterbalanced the wind-driven transport, might be the result of the larger scale effects
719 of the eddies as illustrated above by the relative transport of an along-shelf line of particles.
720 Coherent eddies move offshore and to the west in the area of Stations D and F, more so than
721 at other stations, which would potentially contribute a sizable non-wind transport at these lo-
722 cations (Fig. 6). In contrast, at station B there is little net translation of eddies, but station B
723 is consistently on the northeast side of cyclonic eddies along the western edge (Fig. 9) where
724 the larger scale flow outside of the eddy is to the northwest.

725 That there is less variability in the residual at the onshore stations, where less eddies were
726 observed, suggests that other processes might be driving the residual transport onshore. Here,
727 differences between the Eulerian wave-driven return flow captured by the ADCPs and the the-
728 oretical Stokes drift vertical structure used to account for it here, or errors in the wave esti-
729 mates themselves [Fewings *et al.*, 2008], might be a key element of the difference. Notably,
730 the magnitude of the residual is consistent ($2000 \pm 200 \text{ m}^2$) at onshore stations A, C, and G,
731 which all span the entire summer, and where the effects of the wave-driven return flow should
732 be larger in relative magnitude. Regardless, compared to the wind-driven exchange both the
733 lateral exchange due to coherent eddies and the large scale lateral variations in the background
734 flow field resulted in significantly more volume exchange than what was predicted or observed
735 due to the wind alone.

736 **5.4 Missing Processes**

737 This study has not addressed the role of lateral variability in leading to the mixing of
738 water properties or driving the flux of quantities (i.e. heat or salt) across the inner shelf [Wilkin,
739 2006; Fewings and Lentz, 2011; Kirincich *et al.*, 2013]. By focusing solely on the potential for
740 volume exchange, the results described here are relevant for understanding the translation of
741 water particles across the shelf independent of potential mixing between water particles. While

742 difficult to constrain with the data available, the mixing of water masses during episodic wind
743 or eddy events would increase the effective exchange above that realized via analysis of the
744 mean (net) transport only. An important source of uncertainty is whether the mixing and ex-
745 change from depth-dependent forcings (i.e. wind-driven upwelling or downwelling) is notably
746 different than the mixing of lateral processes, leading to a larger effect on the transfer of prop-
747 erties across the shelf. Additionally, eddies themselves only account for a fraction of the rel-
748 ative volume exchange present during an eddy due to both the definition of an eddy and the
749 conditions that lead to eddy formation. Thus, the role of incoherent small-scale features on
750 horizontal exchange and stirring is a critical component that is missing from this analysis.

751 This work does not address the potential vertical advection by the submesoscale features
752 that comprise most of the small scale coherent eddies found here. As shown by *Kirincich* [2016],
753 inner-shelf eddies have measurable levels of surface convergence and divergence that suggest
754 vertical motions of 1-3 m per day. While this is potentially small relative to areas with stronger
755 upwelling [i.e. *Kirincich et al.*, 2005], given the fluctuating wind forcing observed, it may be
756 an important contribution. Ongoing efforts with this dataset are examining the role of inco-
757 herent stirring on exchange across the inner shelf as well as the implications on the flux of
758 heat and salt through the inner shelf.

759 **6 Summary and Conclusions**

760 Numerous sources of lateral variability exists over the inner-shelf south of Martha's Vine-
761 yard. Depth-dependent wind-driven across-shelf transport varied both in the magnitude and
762 the direction of the exchange over relatively short spatial scales (10-15 km). While forcing from
763 the across-shelf wind tended to dominate the across-shelf wind-driven response onshore at the
764 15-m isobath, the response at the 25-m isobath was complicated by changes in the alignment
765 of the principal axis of flow and potentially, the proximity to bathymetric features. Subme-
766 soscale eddies with scales generally smaller than 10 hours and 6 km were frequently found
767 over the inner shelf with vertical depths of 5-10 m. Eddies tended to occur in key areas along
768 the south coast of Martha's Vineyard including along the western edge of the island, south and
769 west of Wasque Shoals located to the east, and more generally offshore and removed from di-
770 rect topographic influence. The occurrence of eddies was related to a combination of tidal and
771 intermittent wind forcing effects onshore, but appears more due to buoyancy variability off-
772 shore. At slowly varying time-scales of months or longer, strong spatial variability existed in

773 the inner shelf circulation due to the influence of the tides, bathymetry, seasonally varying winds,
774 and stratification.

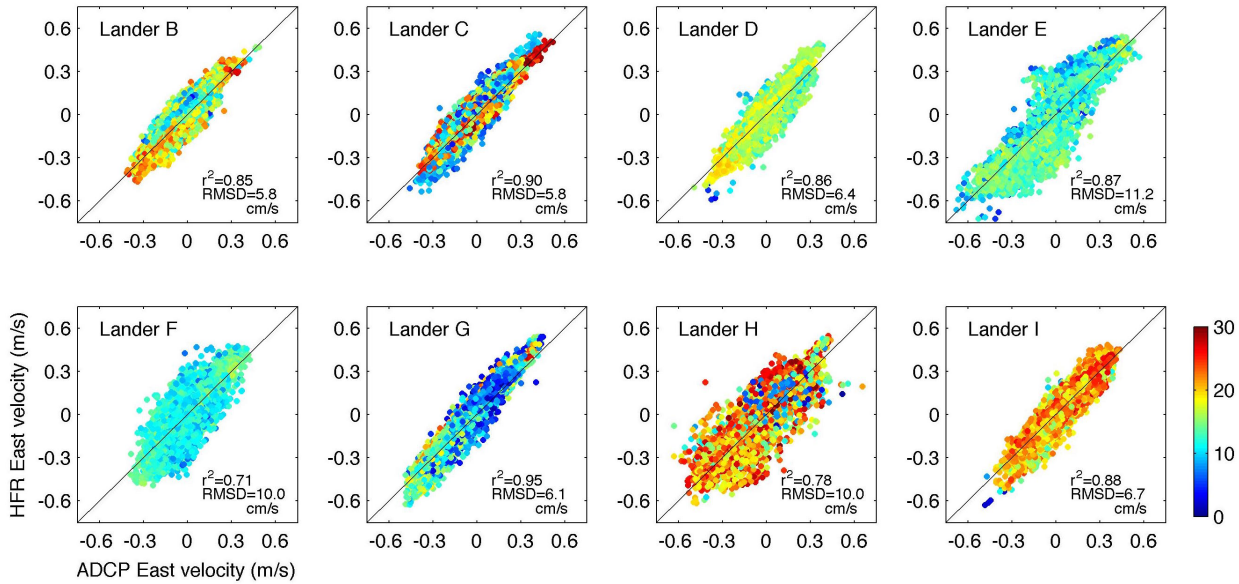
775 The total exchange across the inner shelf south of Martha's Vineyard, MA was a com-
776 plex combination of wind-driven depth-dependent exchange, transport due to coherent eddies,
777 as well as the effects of a mean background circulation. Due to the short time scales of the
778 fluctuating winds, wind forcing itself had a surprisingly small integrated effect on the along-
779 shelf uniform across-shelf exchange, in terms of the total volume of the inner shelf 'upwelled'
780 over the summer stratified period. Components of the depth-dependent exchange across the
781 inner shelf were generally consistent with wind-driven theory, yet the total observed transport
782 often opposed the wind-driven exchange. The integrated effect of small scale lateral variations
783 suggests that lateral exchange due to coherent eddies can make an important contribution to
784 volume transport across the inner shelf on all inner shelves, but especially near areas of com-
785 plex topography.

786 **A: Surface Current Data Quality**

787 The quality of the surface current observations were assessed in multiple ways. First,
788 comparisons were made between the velocity in the surface-most bin of the ADCPs (at 2-4
789 m depth) and the nearest spatial average of the HF radar velocity, measuring the top 0.5 m [*Stew-*
790 *art and Joy, 1974*]. While real differences exist between the two measurement types due to
791 the separation distance and spatial extent [*Graber et al., 1997; Shay et al., 2007*], ADCP to HF
792 radar comparisons are often used to identify whether significant differences between these ob-
793 servations exist that might be due to instrumental noise or bias [see review by *Paduan and*
794 *Washburn, 2013*]. For the 30-min averaged east velocity component, these comparisons, as rms
795 differences range from 6 to 10 cm s^{-1} (Fig. A.1). RMS differences were generally smaller
796 inshore and to the west, with Stations C and B having the smallest differences, while F and
797 I had largest differences, driven in part by the strong spatial variability in tidal velocities that
798 existed along the eastern edge of the study area [*Kirincich et al., 2013*].

799 Secondly, two mass drifter releases within the study period were used by [*Rypina et al.,*
800 *2016*] to make both Eulerian and Lagrangian comparisons between the drifter velocities and
801 trajectories and that possible from the HF radar results. Eulerian comparisons between the drifter
802 velocities and radar velocities had mean bias of 1-4 cm s^{-1} and std dev of 4-7 cm s^{-1} . La-
803 grangian comparisons between the drifter trajectories and pseudo-trajectories launched within

804 the HF radar field had mean separation speeds of $2.5\text{--}5\text{ cm s}^{-1}$. Importantly, these results var-
 805 ied systematically between the releases with the release during stronger wind forcing having
 806 smaller differences, likely due to environmental conditions favoring larger spatial scales of vari-
 807 ability that were better resolved by the radar [Rypina *et al.*, 2014, 2016].



808 **Figure A.1.** Comparisons between HF radar surface currents (with 0.25 m effective depth) and the top most
 809 usable depth bin of the ISLE ADCP estimates for the East velocity component only. Results for lander A
 810 are not included as HF radar-based vectors were not available. In all plots, the scatter is colored by a relative
 811 metric of the vector velocity data quality (with arbitrary units) based on the observed signal power.

812 Acknowledgments

813 The 2014 ISLE field study as well as this analysis was supported by NSF OCE grant #1332646
 814 and the Woods Hole Oceanographic Institution. The authors also thank Craig Marquette for
 815 his tireless efforts preparing, deploying, and recovering all of the moored instrumentation as
 816 well as Irina Rypina and Ken Brink for their helpful comments and insight. The raw data used
 817 in this study will be made available at the WHOI data library archive before publication, but
 818 can be accessed before publication by contacting the authors.

819 References

820 Allen, J. (1980), Models of wind-driven currents on the continental shelf, *Annu. Rev. Fluid*
 821 *Mech.*, 12, 389–433.

- 822 Austin, J. A., and S. J. Lentz (2002), The inner shelf response to wind-driven upwelling
823 and downwelling., *J. Phys. Oceanogr.*, *32*, 2171.
- 824 Capet, X., J. C. McWilliams, M. J. Molemaker, and A. F. Shchepetkin (2008), Mesoscale
825 to Submesoscale Transition in the California Current System. Part I: Flow Struc-
826 ture, Eddy Flux, and Observational Tests, *J. Phys. Oceanogr.*, *38*(1), 29–43, doi:
827 10.1175/2007JPO3671.1.
- 828 Castelao, R. M., and J. A. Barth (2006), The relative importance of wind strength and
829 along-shelf bathymetric variations on the separation of a coastal upwelling jet, *J. Phys.*
830 *Oceanogr.*, *36*, 412–425.
- 831 Chelton, D. B., M. G. Schlax, and R. M. Samelson (2011), Global observa-
832 tions of nonlinear mesoscale eddies, *Prog. Oceanogr.*, *91*(2), 167–216, doi:
833 10.1016/j.pocean.2011.01.002.
- 834 Dudas, S. E., B. A. Grantham, A. R. Kirincich, B. A. Menge, J. Lubchenco, and J. A.
835 Barth (2009), Current reversals as determinants of intertidal recruitment on the central
836 Oregon coast, in *ICES J. Mar. Sci.*, vol. 66, pp. 396–407, doi:10.1093/icesjms/fsn179.
- 837 Fewings, M., and S. J. Lentz (2011), Summertime cooling of the shallow continental
838 shelf, *J. Geophys. Res.*, *116*(C07015), doi:10.1029/2010JC006744.
- 839 Fewings, M., S. J. Lentz, and J. Fredericks (2008), Observations of cross-shelf flow driven
840 by cross-shelf winds on the inner continental shelf., *J. Phys. Oceanogr.*, *38*, 2358–2378,
841 doi:10.1175/2008JPO3990.1.
- 842 Ganju, N. K., S. J. Lentz, A. R. Kirincich, and J. T. Farrar (2011), Complex mean circu-
843 lation over the inner-shelf south of Martha’s Vineyard revealed by observations and a
844 high-resolution model, *J. Geophys. Res.*, *116*(C10036), doi:10.1029/2011JC007035.
- 845 Gordon, R. L. (1996), *Acoustic Doppler Current Profiler: principles of operation, a practi-*
846 *cal primer Second edition for Broadband ADCPs*, 54 pp., RDI Instruments, San Diego,
847 CA.
- 848 Graber, H. C., K. Haus, R. D. Chapman, and L. K. Shay (1997), HF radar comparisons
849 with moored estimates of current speed and direction : Expected differences and impli-
850 cations were collected during the High The average angular difference ranged between,
851 *J. Geophys. Res.*, *102*(97), 18,749–18,766.
- 852 Horwitz, R., and S. J. Lentz (2014), Inner-Shelf Response to Cross-Shelf Wind Stress:
853 The Importance of the Cross-Shelf Density Gradient in an Idealized Numerical Model
854 and Field Observations, *J. Phys. Oceanogr.*, *44*(2008), 86–103, doi:10.1175/JPO-D-13-

- 855 075.1.
- 856 Huyer, A. (1990), Shelf Circulation, in *Sea, v9a*, edited by B. LeMehaute and D. M.
857 Hanes, chap. 12, pp. 1647–1658, John Wiley and Sons.
- 858 Huyer, A., J. H. Fleischbein, J. Keister, P. M. Kosro, N. Perlin, R. L. Smith, and P. a.
859 Wheeler (2005), Two coastal upwelling domains in the northern California Current
860 system, *J. Mar. Res.*, *63*(5), 901–929, doi:10.1357/002224005774464238.
- 861 Kaplan, D. M., and J. Largier (2006), HF radar-derived origin and destination of surface
862 waters off Bodega Bay, California, *Deep Sea Res. Part II Top. Stud. Oceanogr.*, *53*(25-
863 26), 2906–2930, doi:10.1016/j.dsr2.2006.07.012.
- 864 Kim, S. Y. (2010), Observations of submesoscale eddies using high-frequency radar-
865 derived kinematic and dynamic quantities, *Cont. Shelf Res.*, *30*(15), 1639–1655, doi:
866 10.1016/j.csr.2010.06.011.
- 867 Kirincich, A. (2016), The occurrence, drivers, and implications of submesoscale eddies on
868 the Martha’s Vineyard inner shelf, *J. Phys. Oceanogr.*, *46*, 2645–2662, doi:10.1175/JPO-
869 D-15-0191.1.
- 870 Kirincich, A., and J. Barth (2009a), Alongshelf variability of inner-shelf circulation along
871 the central Oregon coast during summer, *J. Phys. Oceanogr.*, *39*(6), 1380–1398, doi:
872 10.1175/2008JPO3760.1.
- 873 Kirincich, A. R., and J. a. Barth (2009b), Time-Varying Across-Shelf Ekman Transport
874 and Vertical Eddy Viscosity on the Inner Shelf, *J. Phys. Oceanogr.*, *39*(3), 602–620,
875 doi:10.1175/2008JPO3969.1.
- 876 Kirincich, A. R., J. A. Barth, B. A. Grantham, B. A. Menge, and J. Lubchenco (2005),
877 Wind-driven inner-shelf circulation off central Oregon during summer, *J. Geophys. Res.*,
878 *110*(C10S03), doi:10.1029/2004JC002,611.
- 879 Kirincich, A. R., T. de Paolo, and E. Terrill (2012), Improving HF radar estimates
880 of surface currents using signal quality metrics, with application to the MVCO
881 high-resolution radar system, *J. Atmos. Ocean. Technol.*, *29*(9), 1377–1390, doi:
882 10.1175/JTECH-D-11-00160.1.
- 883 Kirincich, A. R., S. J. Lentz, J. T. Farrar, and N. K. Ganju (2013), The spatial structure
884 of tidal and mean circulation over the inner shelf south of Martha’s Vineyard, Mas-
885 sachusetts, *J. Phys. Oceanogr.*, *43*(9), 1940–1958, doi:10.1175/JPO-D-13-020.1.
- 886 Kuebel Cervantes, B. T., J. S. Allen, and R. M. Samelson (2003), A modeling study of
887 Eulerian and Lagrangian aspects of shelf circulation off Duck, North Carolina., *J. Phys.*

- 888 *Oceanogr.*, 33(10), 2070–2092.
- 889 Kundu, P. K., and J. S. Allen (1976), Some Three-Dimensional Characteristics of Low-
890 Frequency Current Fluctuations near the Oregon Coast.
- 891 Large, W. G., and S. Pond (1981), Open ocean momentum flux measurements in moderate
892 to strong winds, *J. Phys. Oceanogr.*, 11, 324–336, doi:http://dx.doi.org/10.1175/1520-
893 0485(1981).
- 894 Lentz, S., R. T. Guza, S. Elgar, F. Feddersen, and T. H. C. Herbers (1999), Momentum
895 balances on the North Carolina inner shelf, *J. Geophys. Res.*, 104(c8), 18,205–18,226.
- 896 Lentz, S. J. (1994), Current Dynamics over the Northern California inner shelf, *J. Phys.*
897 *Oceanogr.*, 24, 2461–2478.
- 898 Lentz, S. J. (2001), The Influence of Stratification on the Wind-Driven Cross-Shelf Cir-
899 culation over the North Carolina Shelf*, *J. Phys. Oceanogr.*, 31(9), 2749–2760, doi:
900 10.1175/1520-0485(2001)031.
- 901 Lentz, S. J., and M. R. Fewings (2012), The wind- and wave-driven inner-shelf circula-
902 tion., *Ann. Rev. Mar. Sci.*, 4, 317–43, doi:10.1146/annurev-marine-120709-142745.
- 903 Lentz, S. J., and C. D. Winant (1986), Subinertial currents on the southern California
904 shelf, *J. Phys. Oceanogr.*, 16, 1737–1750.
- 905 Lentz, S. J., M. Fewings, P. Howd, J. Fredericks, and K. Hathaway (2008), Observa-
906 tions and a model of undertow over the inner continental shelf., *J. Phys. Oceanogr.*, 38,
907 2341–2357.
- 908 McGillicuddy, D. J., D. M. Anderson, D. R. Lynch, and D. W. Townsend (2005), Mech-
909 anisms regulating large-scale seasonal fluctuations in Alexandrium Fundyense popula-
910 tions in the Gulf of Maine: Results from a physical-biological model, *Deep Sea Res. II*,
911 52(2698 – 2714), doi:10.1016/j.dsr2.2005.06.021.
- 912 Menge, B. a., J. Lubchenco, M. E. S. Bracken, F. Chan, M. M. Foley, T. L. Freiden-
913 burg, S. D. Gaines, G. Hudson, C. Krenz, H. Leslie, D. N. L. Menge, R. Russell,
914 and M. S. Webster (2003), Coastal oceanography sets the pace of rocky intertidal
915 community dynamics., *Proc. Natl. Acad. Sci. U. S. A.*, 100(21), 12,229–34, doi:
916 10.1073/pnas.1534875100.
- 917 Mitchum, G. T., and A. J. Clarke (1986), The frictional nearshore response to forcing by
918 synoptic scale winds, *J. Phys. Oceanogr.*, 16, 934–946.
- 919 Okubo, A. (1971), Oceanic diffusion diagram, *Deep. Res. II*, 18, 789–802.

- 920 Paduan, J. D., and L. Washburn (2013), High-frequency radar observations of ocean
921 surface currents., *Ann. Rev. Mar. Sci.*, 5, 115–36, doi:10.1146/annurev-marine-121211-
922 172315.
- 923 Pawlowicz, R., B. Beardsley, and S. Lentz (2002), Classical tidal harmonic analysis in-
924 cluding error estimates in MATLAB using T_TIDE, *Comput. Geosci.*, 28(8), 929–937.
- 925 Robinson, I. (1981), Tidal vorticity and residual circulation, *Deep Sea Res. I*, 28(3).
- 926 Rypina, I., A. Kirincich, S. Lentz, and M. Sundermeyer (2016), Investigating the eddy
927 diffusivity concept in the coastal ocean., *J. Phys. Oceanogr.*, 46, 2201–2218.
- 928 Rypina, I. I., A. R. Kirincich, R. Limeburner, and I. A. Udovydchenkov (2014), Eulerian
929 and lagrangian correspondence of high-frequency radar and surface drifter data: effects
930 of radar resolution and flow components, *J. Atmos. Ocean Technol.*, 31(4), 945–966,
931 doi:10.1175/JTECH-D-13-00146.1.
- 932 Shay, L. K., J. Martinez-Pedraja, T. M. Cook, B. K. Haus, and R. H. Weisberg (2007),
933 High-Frequency Radar Mapping of Surface Currents Using WERA, *J. Atmos. Ocean
934 Technol.*, 24(3), 484–503, doi:10.1175/JTECH1985.1.
- 935 Song, Y. T., D. B. Haidvogel, and S. M. Glenn (2001), Effects of topographic variability
936 on the formation of upwelling centers off New Jersey: A theoretical model, *J. Geophys.
937 Res.*, 106(C5), 9223–9240.
- 938 Stewart, R. H., and J. W. Joy (1974), HF radio measurements of surface currents, *Deep.
939 Res.*, 21, 1039–1049.
- 940 Terray, E., R. Gordon, and B. Brumley (1997), Measuring wave height and direction using
941 upward-looking ADCPs, in *Ocean. MTS/IEEE Conf. Proc.*, vol. 1, pp. 287–290, IEEE.
- 942 Tilburg, C. E. (2003), Across-shelf transport on a continental shelf: Do across-shelf winds
943 matter?, *J. Phys. Oceanogr.*, 33, 2675–2688.
- 944 Tilburg, C. E., and R. Garvine (2003), Three-dimensional flow in a shallow coastal up-
945 welling zone: alongshore convergence and divergence on the New Jersey shelf., *J. Phys.
946 Oceanogr.*, 33, 2113–2125.
- 947 Wilkin, J. (2006), The summertime heat budget and circulation of southeast New England
948 shelf waters, *J. Phys. Oceanogr.*, 36, 1997–2011.
- 949 Yankovsky, A. E., and D. C. Chapman (1995), Generation of mesoscale flows over the
950 shelf and slope by shelf wave scattering in the presence of a stable, sheared mean
951 current., *J. Geophys. Res.*, 100(C4), 6725–6742.